LETTER

doi:10.1038/nature13162

Coordination of entorhinal–hippocampal ensemble activity during associative learning

Kei M. Igarashi[1], Li Lu[1], Laura L. Colgin[2], May-Britt Moser[1] & Edvard I. Moser[1]

Accumulating evidence points to cortical oscillations as a mechanism for mediating interactions among functionally specialized neurons in distributed brain circuits[1–6]. A brain function that may use such interactions is declarative memory—that is, memory that can be consciously recalled, such as episodes and facts. Declarative memory is enabled by circuits in the entorhinal cortex that interface the hippocampus with the neocortex[7,8]. During encoding and retrieval of declarative memories, entorhinal and hippocampal circuits are thought to interact via theta and gamma oscillations[4,6,8], which in awake rodents predominate frequency spectra in both regions[9–12]. In favour of this idea, theta–gamma coupling has been observed between entorhinal cortex and hippocampus under steady-state conditions in well-trained rats[12]; however, the relationship between interregional coupling and memory formation remains poorly understood. Here we show, by multisite recording at successive stages of associative learning, that the coherence of firing patterns in directly connected entorhinal–hippocampus circuits evolves as rats learn to use an odour cue to guide navigational behaviour, and that such coherence is invariably linked to the development of ensemble representations for unique trial outcomes in each area. Entorhinal–hippocampal coupling was observed specifically in the 20–40-hertz frequency band and specifically between the distal part of hippocampal area CA1 and the lateral part of entorhinal cortex, the subfields that receive the predominant olfactory input to the hippocampal region[13]. Collectively, the results identify 20–40-hertz oscillations as a mechanism for synchronizing evolving representations in dispersed neural circuits during encoding and retrieval of olfactory–spatial associative memory.

Neural activity was recorded from entorhinal cortex (EC) and CA1 of 17 rats trained to solve a simplified version of an odour–place association task thought to depend on interfacing of the hippocampus with inputs from the olfactory bulb and the piriform cortex via the EC[13–15] (Fig. 1 and Supplementary Video 1). On each trial, the animal sampled odours in a cue port for 1 s and then, depending on odour identity, ran to either of two cups for food reward (Fig. 1b). Following 3 weeks of training, the percentage of correct trials increased to asymptotic levels, reaching a criterion of two consecutive sessions of 85% correct performance after 16.8 ± 0.8 days (mean ± s.e.m.; Fig. 1c; repeated measures analysis of variance (ANOVA): $F(20, 320) = 95.6$, $P < 0.001$). Training-day numbers 2, 6, 10, 14 and 18 were defined as T1–T5, respectively. T5 was post-criterion for all animals.

We first examined spectral activity in CA1 of five well-trained animals. After these animals had reached the 85% performance criterion, electrodes were implanted across the transverse axis of CA1 (Fig. 1a and Extended Data Fig. 1a). Analyses focused on activity during the cue-sampling period, when recall of odour–place associations was expected to be initiated (Fig. 1d and Extended Data Fig. 2). Cue sampling was associated with strong oscillatory activity in the local field potential (LFP) of CA1 (Fig. 1e). The activity change was strongest in the 20–40-Hz frequency range, below the gamma-band frequencies that dominate running behaviour[10,12,16] and in agreement with previous observations in olfaction-based discrimination tasks[15]. Some increase was observed at ~15–20 Hz, but a 20-Hz cut-off was used to avoid confounds with theta harmonics (~14–18 Hz; Fig. 1e and Extended Data Fig. 3). The power of the 20–40-Hz oscillation increased gradually during the cue sampling interval, peaked during the second half, and dropped back as soon as the animal left the port (Fig. 1e, f, and Extended Data Figs 3 and 4). The magnitude of this oscillation increased from proximal to distal CA1 (dCA1; Extended Data Fig. 5), consistent with the idea that beta-frequency olfactory inputs mediated by the lateral part of the EC (LEC) preferentially reach dCA1[13,15].

We next asked whether 20–40-Hz oscillations in dCA1 are accompanied by similar LFP activity in EC. In 9 rats, we recorded simultaneously from dCA1 and layer III of either lateral or medial EC (LEC: $n = 20$ tetrode pairs in 5 rats; MEC: $n = 16$ tetrode pairs in 4 rats; Extended Data Fig. 1a–c). In all animals that reached the 85% criterion, LEC exhibited strong 20–40-Hz oscillations during cue sampling (Fig. 1g and Extended Data Fig. 3). These oscillations were highly coherent with 20–40-Hz oscillations in dCA1 (Fig. 1h, i). Both power and coherence reached peak values during the second half of the cue interval (Fig. 1g, h). Coherence was increased only rarely during the inter-cue period (Fig. 1f, j, k). The changes were restricted to LEC. No increase in 20–40-Hz oscillations was detected in MEC (Fig. 1g), and oscillations in dCA1 showed stronger coupling with LEC than MEC at all 0.97-Hz frequency bins between 15.6 and 39.0 Hz but not at any lower or higher frequencies (false discovery rate (FDR) corrected for 62 multiple comparisons at 0–60 Hz, $q < 0.05$; Fig. 1h, i). Instead, and in agreement with previous results[12], the MEC electrodes showed fast gamma oscillations that coupled moderately with dCA1 during the running segments of the task (peak frequency at 72.1 and 61.0 Hz for power and coherence, respectively; Extended Data Fig. 3).

The observed 20–40-Hz coherence between LEC and CA1 could reflect disynaptic LEC–CA3 and CA3–CA1 coupling[12]. If this were the case, LEC–CA1 coherence would be expressed in both proximal CA1 (pCA1) and dCA1, considering that LEC input terminates indiscriminately along the CA3 transverse axis[13]. However, simultaneous recordings from LEC and pCA1 showed no increase in coherence during the cue interval (3 rats; Fig. 1h). At all frequencies from 13.7 to 33.2 Hz, pCA1–LEC coherence was weaker than dCA1–LEC coherence in the first group of rats (FDR corrected, $q < 0.05$; 12 tetrode pairs; Fig. 1i). The lack of coupling between LEC and pCA1, and between MEC and dCA1, suggests that the coherence is mediated by direct LEC–CA1 connections.

We then asked whether and how oscillatory coupling between LEC and dCA1 evolves as the animals learn to use the odour cues to navigate. Tetrodes were targeted simultaneously to dCA1 and layer III of LEC in 5 rats. Once the electrodes were in place, the rats were trained to associate different odours with different reward locations, and LFP as well as individual cell activity were recorded daily from each region, from T1 to T5. Learning was accompanied by a steady increase in 20–40-Hz coherence between LEC and dCA1 (Fig. 2a–c and Extended Data Fig. 6g; repeated measures ANOVA for all 20 combinations of recording pairs: $F(4, 76) = 35.7$, $P < 0.001$; one recording pair per animal: $F(4, 16) = 17.9$, $P < 0.001$). At T5, LEC–dCA1 coherence was stronger

[1]Kavli Institute for Systems Neuroscience and Centre for Neural Computation, Norwegian University of Science and Technology, Olav Kyrres gate 9, MTFS, 7491 Trondheim, Norway. [2]Center for Learning and Memory, The University of Texas at Austin, Austin, Texas 78712-0805, USA.

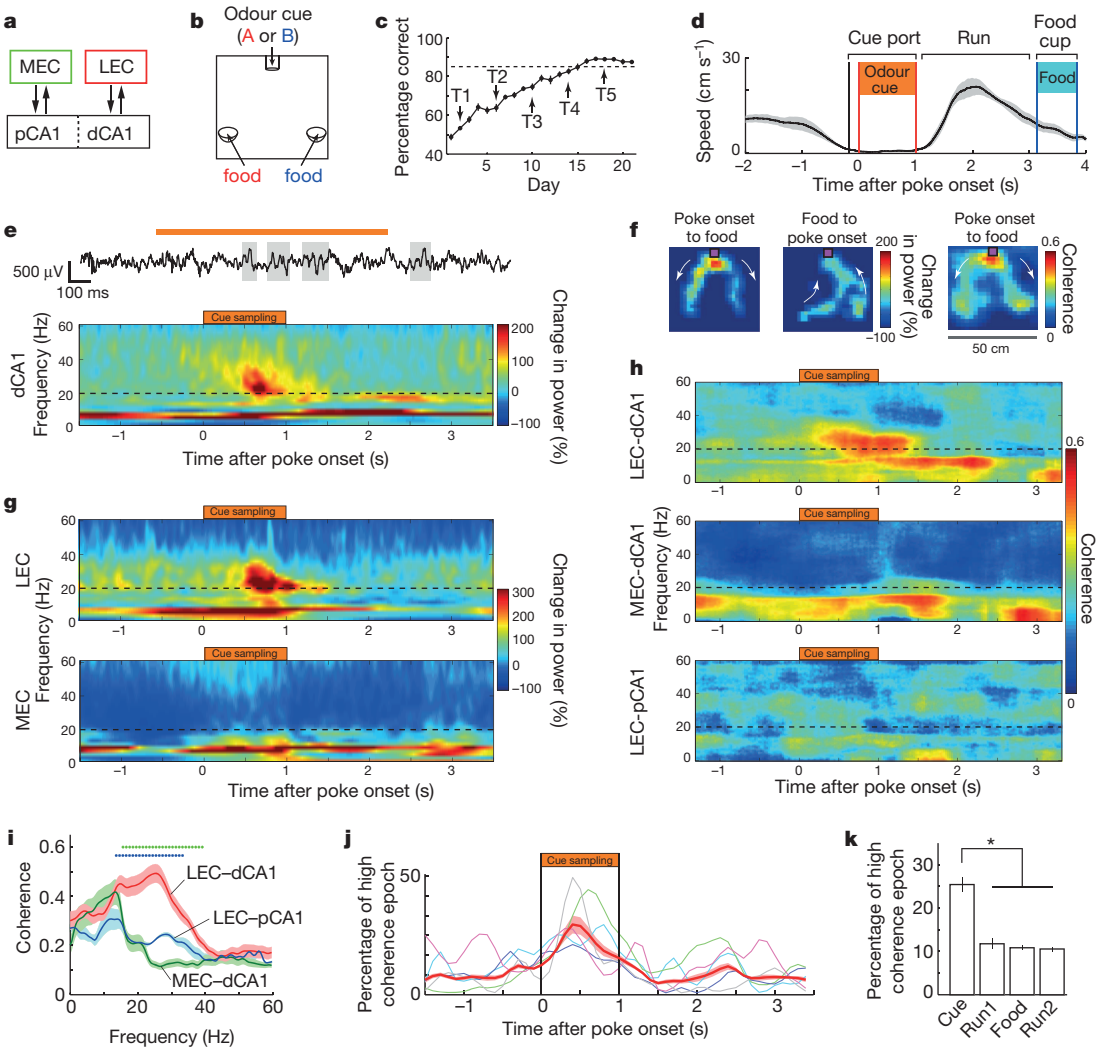

Figure 1 | 20–40-Hz coupling between LEC and dCA1 during successful odour discrimination. **a**, Box diagram showing recording locations and their connections. **b**, Task chamber. **c**, Correct choice rate (mean ± s.e.m.) as a function of training day (all animals). **d**–**k**, Data from T5. **d**, Mean speed ± s.e.m. (shading) before, during and after odour cue. **e**, Top, example trace of local field potential (LFP) from dCA1. Orange bar, cue period. Grey shadings indicate 20–40-Hz oscillations with power >2s.d. above the mean. Bottom, time-resolved power spectrum averaged across dCA1 tetrodes (all animals). LFP power was normalized to pre-cue power and aligned to cue onset ($t = 0$). Note increase in 20–40-Hz oscillation during cue sampling ($t(8) = 3.3$, $P = 0.01$, paired t-test). **f**, Map of task chamber showing spatial distribution of 20–40-Hz power change between cue sampling and food retrieval (left) and between food retrieval and cue sampling (middle). Right, spatial distribution of 20–40-Hz LEC–dCA1 coherence (cue sampling to food retrieval). **g**, Time-resolved power spectra averaged across all tetrodes of all rats in LEC ($t(9) = 4.8$, $P < 0.001$) and MEC ($t(7) = 1.3$, $P = 0.24$). **h**, Time-resolved coherence spectra averaged over all recording pairs in LEC–dCA1, MEC–dCA1 and LEC–pCA1. Odour-evoked 20–40-Hz coupling is apparent in LEC–dCA1 (cue versus pre-cue: $t(19) = 4.4$, $P < 0.001$) but not in MEC–dCA1 or LEC–pCA1. **i**, Mean coherence ± s.e.m. (shading) as a function of frequency for all LEC–dCA1, MEC–dCA1 and LEC–pCA1 recording pairs in all animals. Green and blue dots at the top indicate frequencies with significant LEC–dCA1 versus MEC–dCA1 and LEC–dCA1 versus LEC–pCA1 differences, respectively ($q < 0.05$, FDR corrected, all tetrode pairs). **j**, Percentage of high 20–40-Hz LEC–dCA1 coherence as a function of trial time (mean ± s.e.m. of all recording pairs). 100-ms blocks with coherence exceeding 2s.d. of coherence across the entire session were defined as high-coherence epochs. Pale coloured lines, individual rats. **k**, Percentage of high-coherence epochs during cue sampling (cue), running (run1, to food cup; run2, back to cue port), and at food cup (food) (repeated-measures ANOVA: $F(3, 57) = 36.0$, $P < 0.001$; *$P < 0.001$, Bonferroni post-hoc test).

than at T1 for each 0.97-Hz frequency bin between 15.6 and 43.0 Hz (Fig. 2b, c; FDR corrected for 62 multiple comparisons at 0–60 Hz, $q < 0.05$). Coherence in the theta-band showed no change (Fig. 2c; $F(4, 76) = 0.79$, $P = 0.54$). The development of interregional coupling was accompanied by gradual cross-frequency coupling between theta and 20–40-Hz oscillations in dCA1 (Fig. 2d–g; repeated measures ANOVA for mean vector length of 20–40-Hz event distribution across theta phase: $F(4, 36) = 36.6$, $P < 0.001$), supporting earlier observations in CA3 in an item-context association task[17]. In LEC, by contrast, 20–40-Hz and theta oscillations were phase-coupled from the start of training (Extended Data Fig. 7). In both regions, the power of the 20–40-Hz oscillations remained unaltered (Extended Data Fig. 6a–d), suggesting that learning is primarily associated with increased coupling of pre-existing 20–40-Hz rhythms.

To determine whether coupling of 20–40-Hz oscillators in LEC and dCA1 is necessary for successful performance, we assessed activity at T5 on error trials ('T5e'; Supplementary Video 1). Results were compared to an identical number of correct trials from the same session (down-sampled correct trials, 'T5d'). The coherence of LEC and dCA1 oscillations in the 20–40-Hz band decreased significantly on error trials (Fig. 2a–c; paired t-test for all combinations of recording pairs, $t(19) = 9.81$, $P < 0.001$; for one pair per animal: $t(4) = 5.0$, $P = 0.007$). There was also a decrease in cross-frequency coupling in dCA1 (Fig. 2f, g; $t(9) = 6.30$, $P < 0.001$). These findings suggest that 20–40-Hz coupling of dCA1 and LEC is necessary for successful odour-based navigation.

The emergence of 20–40-Hz coupling was reflected in individual dCA1 and LEC cells. A large proportion of the cue-port cells[18] in dCA1 were

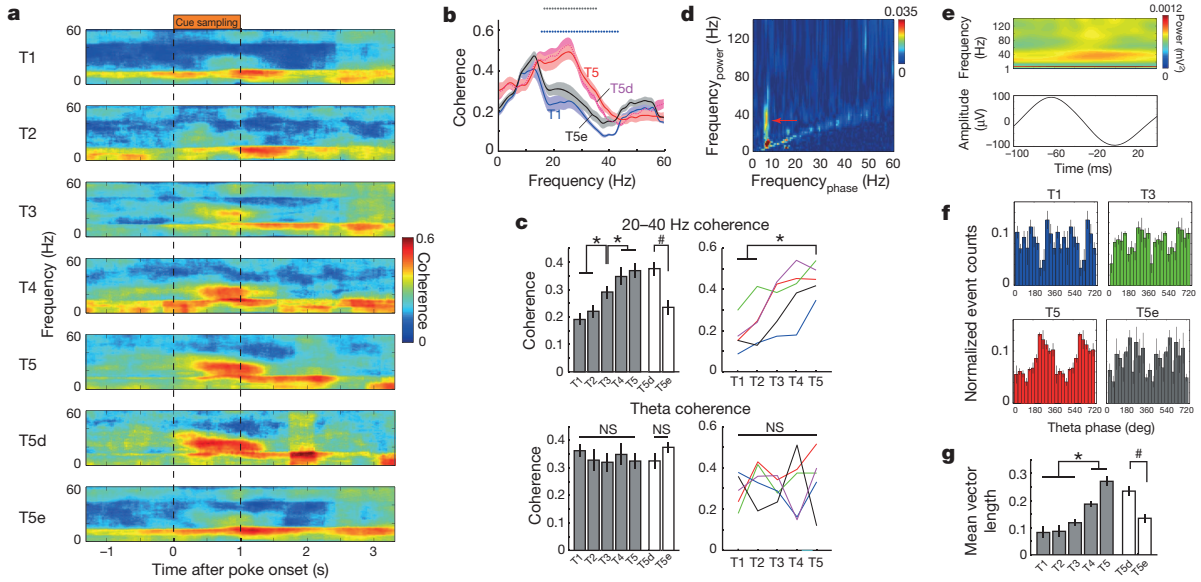

Figure 2 | Evolution of 20–40-Hz coupling between LEC and dCA1 during odour–place learning. **a**–**c**, Coherence between LEC and dCA1 evolves in parallel with learning (average of 20 recording pairs in 5 rats). **a**, Time-resolved LEC–dCA1 coherence spectra. **b**, Mean coherence ± s.e.m. as a function of frequency. Top, blue and grey dots indicate frequencies at which T1–T5 and T5d–T5e differences, respectively, were significant ($q < 0.05$, FDR corrected). **c**, Coherence for 20–40-Hz (top) and theta frequencies (bottom) from T1 to T5 and on T5 error trials (T5e). T5d, correct T5 trials after down-sampling to same number of trials as T5e. Left, mean coherence ± s.e.m. (*$P < 0.05$, Bonferroni post-hoc test; $^{\#}P < 0.05$, paired t-test); right, individual animals (colour-coded). **d**, Example cross-frequency coherence plot showing that 20–40-Hz oscillatory power (y-axis) was modulated by theta phase (x-axis) in dCA1 at T5. Coupling strength is colour-coded. **e**, Top, time-resolved power spectrum averaged across all theta cycles with 20–40-Hz oscillations ($t = 0$, theta trough). Bottom, averaged unfiltered theta cycle. **f**, Theta phase distribution of 20–40-Hz oscillation maxima for LFP from dCA1 (mean ± s.e.m.; 0°, trough). **g**, Mean vector length of distributions in **f** (T1 to T5 and T5e). *P and $^{\#}P$ as in **c**.

place cells (Extended Data Fig. 8). The proportion of cue-port cells with spike activity significantly phase-locked to local 20–40-Hz oscillations increased from 19% to 42% in dCA1, and from 22% to 65% in LEC (T1 and T5, respectively; Extended Data Fig. 9; binomial tests with Bonferroni correction, $P < 0.005$). In dCA1, the phase-locking was reduced on error trials (T5e versus T5d: $P = 0.03$, LEC: $P = 0.097$). There was also an increase from T1 to T5 in cross-regional phase locking (from 7.9% to 17.4% for dCA1 cells versus 20–40-Hz LEC oscillations; from 13.3% to 24.4% for LEC cells versus dCA1 oscillations; both $P < 0.005$; Extended Data Fig. 9). The match between oscillatory coupling in LFP and individual neurons suggests that the change occurred locally in LEC and dCA1.

To establish whether oscillatory coupling evolved as a reflection of changes in the animals' motor behaviour, we monitored the path of the rats. There was no change in position and head direction before, during or after cue sampling (Extended Data Fig. 2a–f). Power and coherence in dCA1 and LEC, as well as 20–40-Hz–theta cross-frequency coupling, were significantly larger during the cue interval than during immobility at other times (Extended Data Fig. 4), suggesting that the 20–40-Hz activity at the cue port is independent of relationships between speed and gamma frequency[19].

Could the coupling reflect other non-specific behavioural changes, such as enhanced attention to the odour stimuli, which might be accompanied by increased power and coherence of beta-gamma oscillations[20,21]? To dissociate memory from attention, we conducted two control tasks, each designed to maintain attention but disrupt memory-based performance. In both tasks, attention was operationalized by monitoring the sniffing frequency of the rat during the cue interval at T5 (Extended Data Fig. 2 g–i). In the first test, we added, for each animal, a set of non-cued trials (T5n) in which only clean air was delivered at the odour port. The increase in 20–40-Hz power was blocked on these trials (Fig. 3a–c; power: dCA1: $t(8) = 3.50$, $P = 0.008$; LEC: $t(9) = 8.40$, $P < 0.001$), as was the increase in coherence (reduced compared to T5 at all frequencies between 16.6 and 34.2 Hz). Sniffing was maintained (Extended Data Fig. 2n–o). In the second test, we trained 4 of the animals with two additional odour pairs (C/D and E/F). After each switch of odour pairs, performance dropped temporarily, and then reverted back to criterion within three days (Fig. 3d). This development was paralleled by a significant drop in 20–40-Hz coupling between LEC and dCA1 on day 1 (paired t-test for T5 versus day 1: $t(15) = 2.19$, $P = 0.04$) and complete recovery by day 3 ($F(2, 30) = 4.05$, $P = 0.03$ for C/D and $F(2, 30) = 4.54$, $P = 0.02$ for E/F) (Fig. 3e and Extended Data Fig. 6e, f). There was no change in sniffing frequency during the change of odour pairs ($t(3) < 0.5$, $P > 0.6$; Extended Data Fig. 2p). These two series of observations suggest that 20–40-Hz coupling was not primarily a reflection of attention.

In a final set of analyses, we examined if the changes in spike timing were accompanied by changes in the subset of cells recruited by each odour. In both dCA1 and LEC, a substantial fraction of the cells developed selectivity for one of the odours (Fig. 4a–c). 'Selectivity' was expressed for each cell as the difference in firing rate during each odour divided by the sum of these rates. On individual trials, average selectivity increased during the cue period, mirroring the development of 20–40-Hz oscillations (Fig. 4a). The development of unique representations for left and right odours was confirmed by population vector analysis (Fig. 4b, c) as well as receiver-operating characteristic (ROC) analysis (Extended Data Fig. 10). Significant changes in selectivity were not observed in pCA1 or MEC (data not shown). The selectivity of the dCA1 and LEC representations was nearly abolished on error trials and non-cued trials (Fig. 4a–c and Extended Data Fig. 10). When a new odour pair was introduced, the representations became non-selective but reverted to fully discriminative levels by day 3, in parallel with correct behavioural choices (Fig. 4f), suggesting that expression of odour-specific representations in dCA1 and LEC is necessary for successful use of odour cues to guide navigation.

The development of odour-selective representations in dCA1 and LEC was strongly correlated with 20–40-Hz coupling between the two regions (Fig. 4d; T1–T5 × 5 animals, all $r > 0.48$, $P < 0.05$). LEC selectivity, 20–40-Hz coupling and task performance developed in parallel whereas selectivity in dCA1 lagged behind (Fig. 4e). A repeated measures ANOVA on normalized values for each variable, with T1 set to 0

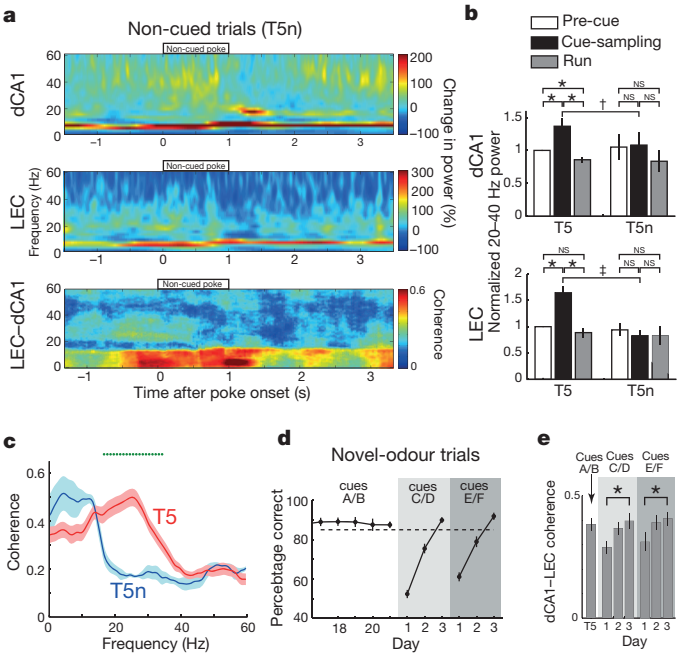

Figure 3 | 20–40-Hz coupling on non-cued trials and novel-odour trials. **a**, Time-resolved power and coherence spectra on non-cued (T5n) trials, averaged across all tetrodes and animals and normalized to the pre-cue period. Top, power for dCA1; middle, power for LEC; bottom, time-resolved coherence spectra for LEC–dCA1. **b**, Normalized power of 20–40-Hz oscillations for cued (T5) and non-cued (T5n) trials (*$P < 0.05$; †$P < 0.01$; ‡$P < 0.001$). **c**, Mean of T5 and T5n coherence spectra for the cue period. Dots indicate frequencies with significant difference ($q < 0.05$, FDR corrected). **d**, Task performance with novel odour pairs (C/D, followed by E/F). **e**, Coherence averaged across the 20–40-Hz band during cue sampling on successive days with novel odours.

and T5 to 1, showed a significant main effect for trials T2–T4 ($F(3, 16) = 9.16$, $P = 0.001$) and no interaction with trial number: $F(6, 32) = 0.69$, $P = 0.66$). Bonferroni post-hoc tests were non-significant for all combinations of task performance, LEC–dCA1 coupling and LEC selectivity, but significant at $P < 0.01$ for all comparisons with dCA1 selectivity, suggesting that LEC triggers the changes in spike timing in the hippocampus.

The observation of 20–40-Hz oscillations in the hippocampus is consistent with reports of such activity during odour discrimination[15] and free running in novel[22] or familiar[12] environments. However, the interaction of these rhythms with external cortical networks and the function of such interactions in memory have remained elusive. Using a hippocampus-dependent associative discrimination task, we have shown that learning is accompanied by coupling of 20–40-Hz oscillations in

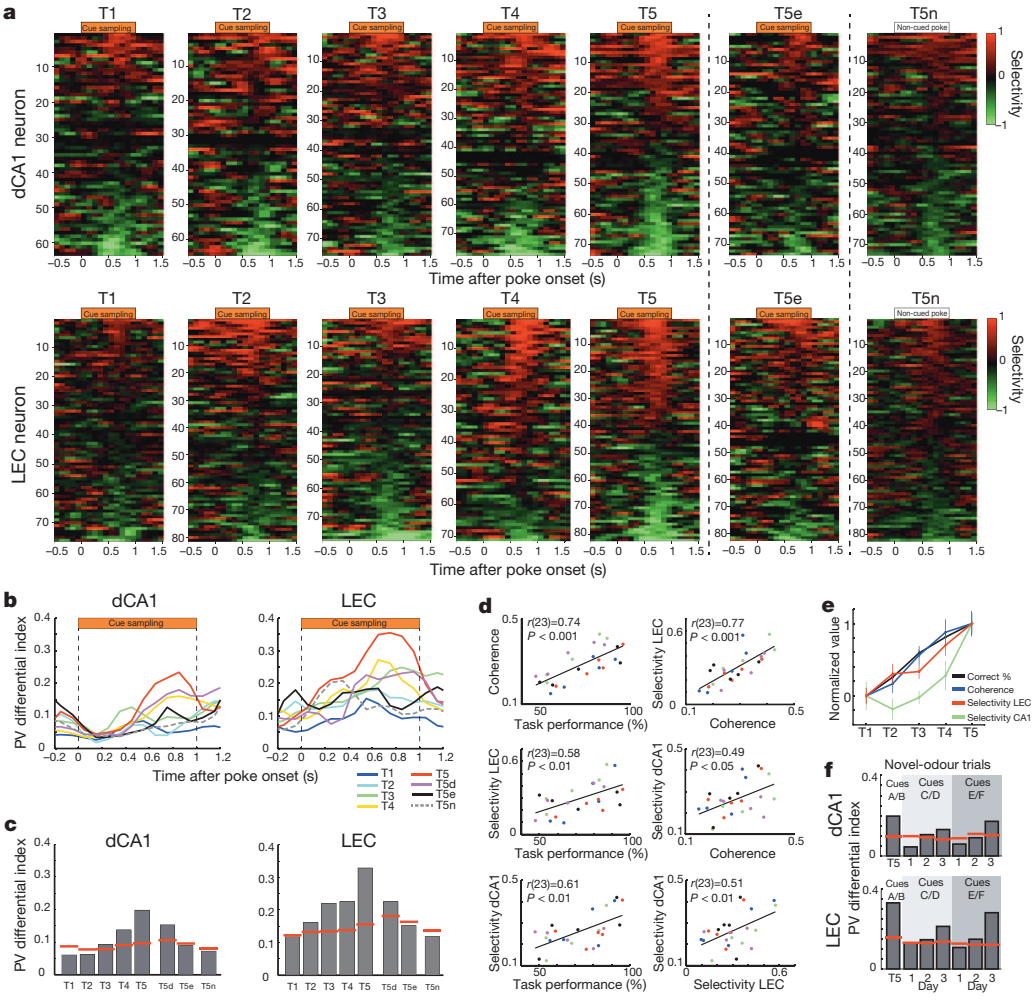

Figure 4 | Development of odour-specific representations in dCA1 and LEC cells. **a**, Response of all cue port cells in dCA1 at T1–T5, T5e and T5n. Each row shows data for one cell around the time of odour sampling. Top, dCA1 cells; bottom, LEC cells. Selectivity for odour cues is expressed for each cell as the difference in firing rate in the presence of left- and right-associated odours, divided by the sum of these rates. Selectivity is colour-coded (–1 and +1 indicate complete selectivity for right and left, respectively). Cells are sorted according to selectivity. **b**, Population vector (PV) analysis across 100-ms time bins for all dCA1 and LEC cells with cue-port activity at T1–T5, T5e and T5n. T5d as in Fig. 2c. Correlations on left and right trials are scaled and shown as a PV differential index (PDI; 0 indicates identical left–right pattern). **c**, Averaged PDIs for second half of odour interval. Red lines indicate 95th percentiles from shuffled distributions at each time point. **d**, Correlation between task performance (correct choice rate; Fig. 1c), LEC–dCA1 coherence at 20–40 Hz (Fig. 2c), and mean selectivity of dCA1 and LEC cells (Fig. 4a). Each dot represents averaged data for a single animal at one time point (5 rats × 5 time points). Colours indicate rat identities. **e**, Development of task performance, coherence and selectivity in dCA1 and LEC. Variables are normalized onto a scale from 0 (T1) to 1 (T5) (mean ± s.e.m.; $n = 5$ rats). **f**, PDIs for trials with novel odour pairs.

connected cell populations of LEC and dCA1, and that, in each of these areas, such coupling coincides with the formation of unique odour representations. Error trials and change of odour contingencies were invariably accompanied by reduced coupling and reduced ensemble selectivity, suggesting that the changes are necessary for successful retrieval or retrieval-based navigation. The results identify 20–40-Hz coupling as a potential mechanism for the evolution of functional circuits during encoding of associative memory in entorhinal–hippocampal systems. Coherent firing between LEC and CA1, timed by 20–40-Hz oscillations, may be a prerequisite for the formation of distinct representations for differentially associated odour cues, both because coupling provides sufficient coincidence of pre- and postsynaptic activity for synaptic strengthening to take place[3,23] and because coincident firing among afferent neurons facilitates such strengthening[24]. Interregional coupling may facilitate the pattern-completion processes required for successful reactivation of newly formed entorhinal and hippocampal cell ensembles.

20–40-Hz oscillations occur widely across the cortex[20,25]. During olfactory learning, 20–40-Hz oscillations may coordinate activity across distributed areas spanning from the olfactory bulb to the LEC and the hippocampus. Increases in 20–40-Hz rhythms in the olfactory bulb and olfactory cortex have been observed after olfactory learning[15,26], in parallel with 20–40-Hz field oscillations in the hippocampus[15]. Widespread 20–40-Hz oscillations have also been observed to emerge at late stages of habit learning in the ventromedial striatum[27]. Because 20–40-Hz oscillations can maintain synchrony with larger conduction delays than faster gamma oscillations[3,28], they are particularly suitable for linking activity across widely distributed brain regions such as those participating in olfaction-based memory formation. The strong coincidence of entorhinal–hippocampal 20–40-Hz coupling and the emergence of olfactory neural representations in LEC and dCA1, in parallel with behavioural learning, points to 20–40-Hz oscillations as a key ingredient of the mechanism for induction and expression of long-term memory in distributed cortical circuits.

METHODS SUMMARY

Seventeen male Long-Evans rats were trained to perform an odour–place association task. The rats sampled odours for 1 s in an odour port, after which food was delivered in one of two food cups whenever the rat chose the food cup associated with the presented odour. The food cups were placed at the other end of the test chamber. Behavioural testing was controlled by custom software triggering the valves of the olfactometer as well as food-delivery.

The rats were implanted either with a 'hyperdrive' carrying 14 tetrodes targeted to cover almost the entire proximodistal extent of dorsal CA1 ($n = 5$ rats), or with two 'microdrives' carrying 4 tetrodes targeted, respectively, to the distal part of CA1 and either the anterodorsal part of LEC (5 rats) or the dorsal part of MEC (4 rats). In three rats, microdrives were targeted simultaneously to LEC and the proximal part of CA1. A multi-tetrode parallel recording system (Neuralynx or Axona) was used to obtain local field potentials and spike activity from individual cells, to monitor animal behaviour, and to time odour and food delivery. In rats with implants in dCA1 and LEC, implantation and tetrode turning were performed prior to the main part of the behavioural training (T1 to T5).

Analyses were focused on the 'cue sampling period' during which the rats stood still and actively sampled odour cues at the cue port. Because all animals were trained and tested similarly, there was no randomization or blinding. The experiments were performed in accordance with the Norwegian Animal Welfare Act and the European Convention for the Protection of Vertebrate Animals used for Experimental and Other Scientific Purposes.

Online Content Any additional Methods, Extended Data display items and Source Data are available in the online version of the paper; references unique to these sections appear only in the online paper.

Received 4 July 2013; accepted 17 February 2014.
Published online 16 April 2014.

1. Freeman, W. J. Spatial properties of an EEG event in the olfactory bulb and cortex. *Electroencephalogr. Clin. Neurophysiol.* **44,** 586–605 (1978).
2. Gray, C. M., Konig, P., Engel, A. K. & Singer, W. Oscillatory responses in cat visual cortex exhibit inter-columnar synchronization which reflects global stimulus properties. *Nature* **338,** 334–337 (1989).
3. Singer, W. Synchronization of cortical activity and its putative role in information processing and learning. *Annu. Rev. Physiol.* **55,** 349–374 (1993).
4. Buzsaki, G. *Rhythms of the Brain* (Oxford University Press, 2006).
5. Fries, P. Neuronal gamma-band synchronization as a fundamental process in cortical computation. *Annu. Rev. Neurosci.* **32,** 209–224 (2009).
6. Colgin, L. L. Mechanisms and functions of theta rhythms. *Annu. Rev. Neurosci.* **36,** 295–312 (2013).
7. Squire, L. R. Memory and the hippocampus: a synthesis from findings with rats, monkeys, and humans. *Psychol. Rev.* **99,** 195–231 (1992).
8. Buzsáki, G. & Moser, E. I. Memory, navigation and theta rhythm in the hippocampal-entorhinal system. *Nature Neurosci.* **16,** 130–138 (2013).
9. Buzsáki, G., Leung, L. W. & Vanderwolf, C. H. Cellular bases of hippocampal EEG in the behaving rat. *Brain Res.* **287,** 139–171 (1983).
10. Bragin, A. *et al.* Gamma (40–100 Hz) oscillation in the hippocampus of the behaving rat. *J. Neurosci.* **15,** 47–60 (1995).
11. Chrobak, J. J. & Buzsaki, G. Gamma oscillations in the entorhinal cortex of the freely behaving rat. *J. Neurosci.* **18,** 388–398 (1998).
12. Colgin, L. L. *et al.* Frequency of gamma oscillations routes flow of information in the hippocampus. *Nature* **462,** 353–357 (2009).
13. Witter, M. P. & Amaral, D. G. in *The Rat Nervous System* (ed. Paxinos, G.) 635–704 (Elsevier Academic, 2004).
14. Day, M., Langston, R. & Morris, R. G. Glutamate-receptor-mediated encoding and retrieval of paired-associate learning. *Nature* **424,** 205–209 (2003).
15. Martin, C., Beshel, J. & Kay, L. M. An olfacto-hippocampal network is dynamically involved in odor-discrimination learning. *J. Neurophysiol.* **98,** 2196–2205 (2007).
16. Montgomery, S. M. & Buzsaki, G. Gamma oscillations dynamically couple hippocampal CA3 and CA1 regions during memory task performance. *Proc. Natl Acad. Sci. USA* **104,** 14495–14500 (2007).
17. Tort, A. B., Komorowski, R. W., Manns, J. R., Kopell, N. J. & Eichenbaum, H. Theta-gamma coupling increases during the learning of item-context associations. *Proc. Natl Acad. Sci. USA* **106,** 20942–20947 (2009).
18. Eichenbaum, H., Kuperstein, M., Fagan, A. & Nagode, J. Cue-sampling and goal-approach correlates of hippocampal unit activity in rats performing an odor-discrimination task. *J. Neurosci.* **7,** 716–732 (1987).
19. Ahmed, O. J. & Mehta, M. R. Running speed alters the frequency of hippocampal gamma oscillations. *J. Neurosci.* **32,** 7373–7383 (2012).
20. Fries, P., Reynolds, J. H., Rorie, A. E. & Desimone, R. Modulation of oscillatory neuronal synchronization by selective visual attention. *Science* **291,** 1560–1563 (2001).
21. Buschman, T. J. & Miller, E. K. Top-down versus bottom-up control of attention in the prefrontal and posterior parietal cortices. *Science* **315,** 1860–1862 (2007).
22. Berke, J. D., Hetrick, V., Breck, J. & Greene, R. W. Transient 23–30 Hz oscillations in mouse hippocampus during exploration of novel environments. *Hippocampus* **18,** 519–529 (2008).
23. Bi, G. Q. & Poo, M. M. Synaptic modifications in cultured hippocampal neurons: dependence on spike timing, synaptic strength, and postsynaptic cell type. *J. Neurosci.* **18,** 10464–10472 (1998).
24. McNaughton, B. L., Douglas, R. M. & Goddard, G. V. Synaptic enhancement in fascia dentata: cooperativity among coactive afferents. *Brain Res.* **157,** 277–293 (1978).
25. Engel, A. K. & Fries, P. Beta-band oscillations — signalling the status quo? *Curr. Opin. Neurobiol.* **20,** 156–165 (2010).
26. Ravel, N. *et al.* Olfactory learning modifies the expression of odour-induced oscillatory responses in the gamma (60–90 Hz) and beta (15–40 Hz) bands in the rat olfactory bulb. *Eur. J. Neurosci.* **17,** 350–358 (2003).
27. Howe, M. W., Atallah, H. E., McCool, A., Gibson, D. J. & Graybiel, A. M. Habit learning is associated with major shifts in frequencies of oscillatory activity and synchronized spike firing in striatum. *Proc. Natl Acad. Sci. USA* **108,** 16801–16806 (2011).
28. Kopell, N., Ermentrout, G. B., Whittington, M. A. & Traub, R. D. Gamma rhythms and beta rhythms have different synchronization properties. *Proc. Natl Acad. Sci. USA* **97,** 1867–1872 (2000).

Supplementary Information is available in the online version of the paper.

Acknowledgements We thank A. M. Amundsgård, K. Haugen, K. Jenssen, E. Kråkvik, R. Skjerpeng and H. Waade for technical assistance, and M. Witter and members of the Moser laboratory for discussions. This work was supported by two Advanced Investigator grants from the European Research Council ('CIRCUIT', Grant Agreement no. 232608; 'ENSEMBLE', Grant Agreement no. 268598), the Kavli Foundation, the Centre of Excellence scheme of the Research Council of Norway (Centre for the Biology of Memory and Centre for Neural Computation), the Mishima Kaiun Memorial Foundation, and the Japan Society for the Promotion of Science.

Author Contributions K.M.I., M.-B.M. and E.I.M. designed experiments and analyses; K.M.I. and L.L. performed the experiments; K.M.I. performed the majority of the analyses, with input from L.L.C, M.-B.M. and E.I.M.; K.M.I and E.I.M. wrote the paper with input from all authors.

Author Information Reprints and permissions information is available at www.nature.com/reprints. The authors declare no competing financial interests. Readers are welcome to comment on the online version of the paper. Correspondence and requests for materials should be addressed to E.I.M. (edvard.moser@ntnu.no) or K.M.I. (kei.igarashi@ntnu.no).

METHODS

Subjects. Data were obtained from 17 male Long Evans rats. In 5 of the rats, the tetrodes were implanted along almost the entire proximodistal extent of CA1 using an oval-bundle 'hyperdrive' consisting of 14 independently movable tetrodes[29]. Five of the rats were implanted with two microdrives carrying a single bundle of 4 tetrodes targeted, respectively, to anterodorsal LEC and distal CA1. Four rats were implanted with two microdrives targeted, respectively, to dorsal MEC and distal CA1. Finally, three rats were implanted with two microdrives aimed, respectively, at anterodorsal LEC and proximal CA1. Sample size was determined as the minimal number of animals that would provide statistical power to detect a group difference. We used all animals in which tetrodes hit the target regions. We did not use randomization to allocate animals to experimental treatments and the experimenters were not blind to the identity of the experimental groups.

All animals were 3–5 months old (450–600 g) at the time of implantation. After surgery, they were housed individually in Plexiglas cages (45 × 44 × 30 cm) in a humidity- and temperature-controlled environment. The rats recovered from surgery for at least one week before odour–place training. During training, the rats were put on a food deprivation regimen that kept them at 80–90% of their free-feeding body weight. The animals were kept on a 12-h light/12-h dark schedule. All testing occurred during the dark phase. The experiments were performed in accordance with the Norwegian Animal Welfare Act and the European Convention for the Protection of Vertebrate Animals used for Experimental and Other Scientific Purposes.

Electrode implantation and surgery. Tetrodes were constructed from four twisted 17 μm polyimide-coated platinum-iridium (90%–10%) wires (California Fine Wire). The electrode tips were plated with platinum to reduce electrode impedances to between 150 and 300 kΩ at 1 kHz. During implantation surgery, the animals were anaesthetized with isoflurane. Air flow was kept at 1.2 l min^{-1} with 0.5–3% (v/v) isoflurane as determined by physiological monitoring. Local anaesthetic (Xylocaine) was applied on the skin before making the incision. Holes were drilled on the dorsal skull, after which the rat was implanted with either two microdrives or a hyperdrive. Hyperdrives for CA1 were implanted in the right hemisphere. Microdrives for dCA1/pCA1 and LEC/MEC were implanted in the right and left hemispheres, respectively. Bihemispheric implants were used because layer III EC cells have both ipsi- and contralateral projections to CA1[13,30]. Hyperdrive tetrodes were implanted vertically between AP 3.4 and 4.9 mm, and ML 2.1 and 3.7 mm, relative to bregma in order to cover as much of the proximodistal axis of CA1 as possible[29]. For microdrive implants, one drive was implanted either in the distal or the proximal part of CA1 (AP 4.2, ML 3.3 and AP 3.2, ML 4.0, respectively, distance from brain surface 1.5 mm, tetrode tips pointing medially at an angle of 30° in the coronal plane). The other drive was implanted in either dorsal anterior LEC (AP 6.1, ML 5.0, distance from brain surface 4.5 mm, with tetrode tips pointing laterally at an angle of 16° in the coronal plane) or in the dorsomedial quarter of the MEC (4.5 mm lateral to midline, 0.2–0.3 mm anterior to the transverse sinus, distance from brain surface 1.5 mm, tetrode tips pointing in the anterior direction at an angle of 10° in the sagittal plane). Hyperdrives and microdrives were fixed to the skull with jewellers' screws and dental cement. Two screws inserted above the cerebellum were used as reference and ground electrodes during recordings. For recording of sniffing behaviour, a temperature sensor (a 0.005-inch, Teflon-coated thermocouple, Omega, 5TC-TT-K-36-36) was implanted in the right nostril through a hole made in the dorsal skull. The implant was secured with dental cement. Thermocouples were inserted into the nasal passage through the nasal bone just rostral to the turbinates.

Tetrode placement. Over the course of ~2–3 weeks, the tetrodes were lowered in steps of 200 μm or less until well-separated, large-amplitude, low-frequency neurons appeared in the CA1 pyramidal cell layer or in LEC layer III at a depth of ~7.0 mm. In MEC, tetrodes were targeted at layer III at a depth of ~2.0–4.0 mm. Tetrode positions were maintained across sessions, except in LEC and MEC, where the tetrodes were lowered 100 μm to record from a new set of neurons after the recordings at time point T5 were completed. All tetrode locations were verified histologically at the end (Extended Data Fig. 1). Only animals with tetrodes in the regions of interest were used in this study.

Behavioural task. Cue–place association task. All rats were tested in an odour place association task (Supplementary Video 1). The test box (50 × 50 × 40 cm) contained a cylindrical port for odour delivery ('cue port', 2.9 cm internal diameter, i.d.), and two circular food cups for food delivery (4.5 cm i.d.). Entry and exit from odour ports and food cups were detected via an infrared photo-beam located inside the odour port and the food cups. Three pairs of monomolecular odorants (Sigma-Aldrich) were used as odour cues. Two odours (A/B) were used during the initial stage, of the task (A = isoamyl acetate (banana odour) / B = α-pinene (pine tree odour)). For subsequent stages with novel odours, we used *t*-anethol (anis odour) as C and geraniol (rose odour) as D, and undecanoic γ-lactone (peach odour) as E and benzaldehyde (almond odour) as F. All odours were diluted in mineral oil (Sigma) to a final concentration of 5% (v/v).

Odour cues were delivered using an olfactometer (PHM-275, Med Associates, St. Albans, VT, USA) housed in a shielded box and located next to the behavioural box. Computer-controlled solenoid valves triggered flow of individual channels of odorized air (1.0 l min^{-1}) diluted in charcoal-deodorized air (1.0 l min^{-1}). The odorized air was delivered from the olfactometer to the cue port via Teflon tubing (1.5 mm i.d. × 70 cm). Rats self-initiated each experimental trial by introducing their snout into the cue port. After a random delay of 0.15–0.25 s, either of two odour cues was delivered. The order of odours was altered pseudorandomly across trials. A tone signal was delivered 1.0 s after cue initiation. If the rat stayed in the cue port until the tone signal, food reward was made available in one of the food cups. Odours A, C and E were associated with food in the left cup and odours B, D and F with food in the right cup. Withdrawal of the nose from the cue port terminated the delivery of odour. Rats usually withdrew from the odour port within 1.0–1.5 s and then moved to the cue-associated food cup. If the rat withdrew its nose from the cue port before the tone signal, no food reward was delivered in any of the cups. Correct choices were rewarded with a 45 mg sucrose pellet delivered via a food dispenser (EVN-203-45IR, Med Associates) as soon as the rat broke the photobeam.

Training procedure. Animals were first habituated to the behavioural apparatus and the experimenter for one week and then pre-trained for another week to perform nose pokes at the cue port in the absence of odour cues. Nose poking was followed by running to the food cups and consumption of food rewards. After completion of pre-training, odour cues A/B were introduced in a pseudorandom order during the cue sampling interval and the rats were trained to associate one odour with the left food cup and the other with the right cup by being rewarded only for appropriate choices (Fig. 1b). Training was terminated when the rats reached to a criterion of 85% correct rate for two consecutive sessions (Fig. 1c, 16.8 ± 0.8 days). Days 2, 6, 10, 14 and 18 after odour introduction were defined as time-points T1–T5, respectively (Fig. 1c). The animals were trained on at least two sessions of 30 min daily, usually with ~60 trials per session. Surgery was performed after pre-training. For 5 dCA1-LEC rats, associative training sessions were performed after the tetrodes were in place at the regions of interest.

Non-cued task. After the animals reached the criterion, they were tested in a non-cued control task, in which only flow of vehicle pure air without odour cues was delivered when the animal made the nose poke. After the poke, the animals made random runs to either of the two foods ports, 85% of which were randomly rewarded. Non-cued trials were scheduled after cued sessions each day after the rat had reached the criterion.

Novel cue task. In four rats with simultaneous implants in dCA1 and LECs, training was continued with odour cues C/D, using a similar protocol as for A/B. Criterion was reached within 3 days. The same rats were subsequently trained for cues E/F for another 3 days.

Random foraging task. On each testing day, after the cue–place association task, the rats were tested in a random foraging task in an open field (100 × 100 cm) to estimate spatial tuning of the cells. The rats were trained for at least one session of 10–20 min. Running was motivated by chocolate cereal crumbs or vanilla cookie crumbs thrown randomly into the enclosure.

Data collection. Spike activity was recorded against reference electrodes located at the level of the corpus callosum or higher up for hyperdrive recordings, and against tetrodes with no spike activities in the same region for microdrive recordings. Local field potential (LFP) was always recorded single-ended against a ground in the skull above the cerebellum.

The tetrode drive was connected to a multichannel, impedance matching, unity gain headstage. The output of the headstage was conducted to an Axona acquisition system (Axona Ltd) or to a Neuralynx data acquisition system (Neuralynx) via a lightweight multiwire tether cable and through a slip-ring commutator. Unit activity was amplified by a factor of 3,000–5,000 and band-pass filtered from 800 to 6,700 Hz (Axona) or from 600 to 6,000 Hz (Neuralynx). Spike waveforms above a threshold set by the experimenter (~55 μV) were time-stamped and digitized at 32 kHz (Neuralynx) or 48 kHz (Axona) for 1 ms.

For the hyperdrive recordings in CA1, LFP signals, 1 per tetrode, were recorded in the 0–475-Hz frequency band at a sampling rate of ~2,000 Hz (1,893 Hz sampling and 2,034 Hz sampling for analogue and digital Neuralynx systems, respectively). For the microdrive recordings in dCA1 and LEC, LFP signals from two tetrodes per microdrive were amplified 1,000–3,000 times, lowpass-filtered at 500 Hz, and sampled at a rate of 4,800 Hz (16 bits per sample). This allowed us to analyse the dynamics of oscillatory coherence between dCA1 and LEC for 2 × 2 = 4 'recording pairs' in each animal. In a more restricted analysis, we used only one pair from each animal — the pair that showed the highest power in the 20–40-Hz frequency band (assuming that coherence could be estimated most accurately from this tetrode). Notch filters were not applied. Signals from thermocouples were recorded as described for LFP signals. Light-emitting diodes (LEDs) on the headstage were used to track the rat's movements at a rate of 25 Hz (Neuralynx) or 50 Hz (Axona).

Data analysis. Unless indicated otherwise, analyses were performed using MATLAB code written by the authors. Methods for spectral and wavelet analysis were described previously[12]. Analyses were performed for periods of interest (that is, the cue sampling period at the cue port, runs from cue port to food cups, or runs from food cups to the cue port) during individual trials and then averaged across multiple trials within a session. Unless otherwise indicated, data from the cue sampling period were taken from the second half (500–1,000 ms) to reflect the delayed onset of changes in LFP and spike activity (Figs 1e, g, h and 2a, and Extended Data Fig. 9a, e). Data were normalized against the pre-cue period, when the animal was stationary at the odour port before the cue was delivered (150 to 0 ms before cue onset). To be sure that no odour sampling occurred during the baseline period, we included only trials where the animal's snout was outside the odour port for at least 1 s before the trial. In time-resolved representations, data were averaged by setting the timing of odour cue onset as a trigger. For statistical tests, we used parametric tests since the data did not deviate substantially from a normal distribution. *t*-tests were performed when there was similar variance between groups. s.e.m. are provided for all analyses.

LFP analysis. Time–frequency analysis of power. Time-resolved power across frequencies was computed using a wavelet transform method. Signals were convolved by a family of complex Morlet's wavelets $w(t,f)$, one for each frequency, as a function of time:

$$w(t,f) = A \exp(-t^2/2\sigma_t^2) \exp(2i\pi ft)$$

in which the family of wavelets was characterized by a constant ratio f/σ_f, which was set to 7, and with $\sigma_f = \frac{1}{2}\pi\sigma_t$. The coefficient A was set at:

$$(\sigma_t\sqrt{\pi})^{-1/2}$$

in order to normalize the wavelets such that their total energy was equal to 1.

To control for impedance differences between tetrodes, LFP power was normalized, for each tetrode, to power during the pre-cue period (150 to 0 ms before cue onset) when the animal was stationary at the odour port before the cue was delivered. Normalized power was averaged across trials that did not include prematurely terminated trials (<1 s) during the 1 s period preceding the onset of cue sampling.

Coherence. Coherence was computed using a multitaper method[31] from the Chronux open source MATLAB toolbox (http://chronux.org/). Recordings were cut into non-overlapping, 5 s long windows around the cue sampling event. Results for multiple trials in a single session were averaged. We typically used window sizes of 0.4–1 s and 3–5 tapers. To extract periods of high 20–40-Hz coupling, we first computed time-varying coherence within the 20–40-Hz band using 100-ms bins. Bins were collected when coherence exceeded 2s.d. of the time-averaged coherence.

Bandpass-filtering. An acausal (zero phase shift), frequency domain, finite impulse response bandpass filter was applied to the signals. For theta filtering, 5 and 6 Hz were chosen for stopband and passband, respectively, for low cut-off frequencies; 10 and 11 Hz were chosen for passband and stopband high cut-off frequencies. For filtering of 20–40-Hz oscillations, 18 and 20 Hz were chosen for the stopband and passband, respectively, for the low cut-off frequencies; 40 and 42 Hz were chosen for passband and stopband high cut-off frequencies.

Selection of theta cycles. Theta cycles were selected by bandpass filtering the signal from 6–10 Hz and selecting local minima in the filtered signal (that is, $\theta(t-1) > \theta(t)$ and $\theta(t+1) > \theta(t)$). Segments of the recording were collected and defined as a theta cycle if the time between detected points fell within a range criterion that corresponded to the period of an ~8-Hz theta cycle (that is, 125 ± 25 ms). Local minima of detected theta cycles were required to be separated by at least 100 ms.

Detection of oscillation episodes. To extract periods of 20–40-Hz oscillatory activity in the LFP, we first computed time-varying power within the frequency bands for each recording. Power at each time point was averaged across the 20–40 Hz frequency range to obtain time-varying estimates of oscillatory power. Time points were collected when the power exceeded 2s.d. of the time-averaged power. Time windows, 160 ms in length, were cut around the identified time points. In each 160-ms segment, the maxima of 20–40-Hz oscillatory amplitude were determined from the 20–40-Hz bandpass filtered versions of the recordings. Duplicated 20–40-Hz oscillatory periods, a common consequence of extracting overlapping time windows, were avoided by discarding identical maxima values within a given 20–40-Hz oscillatory subtype and further requiring that maxima of a given subtype be separated by at least 100 ms. Individual 20–40-Hz oscillatory windows were finally constructed from the original, non-bandpass filtered recordings as 400 ms long windows centred around the 20–40-Hz oscillatory amplitude maxima.

Relationship of 20–40-Hz oscillations to theta phase. LFP recordings were bandpass-filtered in the theta range (6–10 Hz), and theta phases for each time point were estimated using the Hilbert transform function from the Signal Processing Toolbox in MATLAB. Theta phases at the time points associated with 20–40-Hz maxima (determined as described above) as well as theta phases for CA1 place cell spikes were collected. Theta phases for each 20–40-Hz oscillatory event were sorted into 30° bins, allowing the phase distribution of each event to be determined. For a given recording, the distributions of 20–40-Hz oscillations were normalized by dividing the bins by the total number of 20–40-Hz oscillatory episodes within a given recording. The normalized distributions were averaged across recordings. In this analysis, and in all analyses involving oscillation phase, the oscillation trough was defined as 0°.

Cross-frequency analysis. The time-varying power in a particular frequency band of the LFP (from 2–200 Hz, in 2 Hz wide frequency bins) was calculated using a Morlet's wavelets technique (see above). Coherence was estimated between the original signal and the time-varying power of the signal for each frequency of interest using the magnitude squared coherence function (Hanning window with 50% overlap; 16,384 and 4,096 FFT points for Axona and Neuralynx data, respectively) from the Signal Processing Toolbox in MATLAB. This provided a measure for determining if power changes at particular frequencies (for example, 20–40 Hz) were correlated with phase at other frequencies (for example, theta).

Time–frequency representation of power across individual theta cycles. Time-varying power in 2-Hz-wide frequency bands, from 2 to 100 Hz, was obtained for individual theta cycles using the wavelet transform method described above. Time frequency representations for multiple theta cycles recorded from the same site and session within the same animal were then averaged.

Prewhitening. For illustrations of power shown in Fig. 2e, a prewhitening autoregressive filter (order of 5) was applied before computation of time frequency analysis to de-emphasize the lower frequency end of the spectrum for illustration purposes. Filter coefficients were estimated using a Yule-Walker approach. Prewhitening was not applied in any of the analyses; it was only used to better visualize power at high frequencies in the selected example above.

Speed–frequency correlation. The relationship between running speed and LFP frequency was estimated following procedures described previously[19]. Briefly, we first calculated the absolute power spectrum of LFP during each 200 ms time window. Relative power was then calculated by determining a *z*-score for each 0.49 Hz frequency bin across successive time windows of individual sessions. Finally, speed was correlated with peak frequency for each speed bin.

Sniffing analysis. Sniffing was measured by thermocouples implanted in the right nostril of the animals[32]. In each breathing cycle, inhalation is associated with decaying voltage output from the thermocouple, and exhalation with increasing voltage output. Signals from the thermocouples were bandpass-filtered at 0.5 and 1.5 Hz for stopband and passband, respectively, for low cut-off frequencies, and at 44.5 and 45.5 Hz for passband and stopband for high cut-off frequencies. Troughs of the signals were detected and the duration of individual sniffs was determined. The inverse of individual sniffing periods was taken as the instantaneous frequency of the sniffing.

Spike analysis. Spike sorting and cell classification. Spike sorting was performed offline using graphical cluster-cutting software described previously[29,33]. Putative excitatory cells were distinguished from putative interneurons by spike width and average rate. Firing rate maps (see below) and head direction tuning curves were used for classification of cell types in MEC[33–36]. Putative excitatory cells with mean firing rates of more than 1.0 Hz (mean firing rate during all left and right cue sampling intervals) were included for further analysis.

Since the tetrodes were not moved during task acquisition, most of the units included in the recordings at time points T1–T5 were from the same cell population. However, occasionally some cells were lost during the course of learning whereas other cells were added, causing slight variation in the number of the cells from session to session (from T1 to T5: between 63 and 75 cells in dCA1 and between 76 and 82 cells in LEC). Cells on error trials (T5e) were from the same population as recorded on correct T5 trials and on down-sampled T5 trials (T5d).

Phase-locking of spikes to 20–40-Hz oscillations. Spikes that occurred during 20–40-Hz oscillatory episodes were selected. For these oscillation-associated spikes, oscillatory phase at the time of spike occurrence was estimated. This was performed by first bandpass-filtering the LFP, performing a Hilbert transform on the filtered signal, and then extracting the phase component at the spike times. Cells were considered to be phase-locked if their phase distribution differed significantly from a uniform distribution ($P < 0.05$, Rayleigh test).

Selectivity index. Odour-specific representation of spikes was assessed using a selectivity metric. Selectivity was computed by comparing firing rates during sampling for left-associated and right-associated cues on successive 100-ms bins:

$$\text{Selectivity} = (\text{FR}_1 - \text{FR}_2)/(\text{FR}_1 + \text{FR}_2)$$

where FR_1 and FR_2 are mean firing rates across multiple trials in individual 100-ms bins during left- and right-associated cue samplings, respectively.

To confirm the results with this difference-over-sum index, we also computed Selectivity using receiver-operating characteristic (ROC) analysis[37], a method based on signal detection theory:

$$\text{Selectivity}_{\text{ROC}} = 2 \times (\text{auROC} - 0.5)$$

where auROC is the area under the ROC curve computed from spike numbers for left and right trials in individual 100-ms bins. auROC = 0.5 indicates that the firing rates were not different between left and right trials; auROC = 1 indicates that firing rates in all left-cue sampling trials were larger than all right-cue sampling trials (see Extended Data Fig. 10).

After scaling, for both Selectivity metrics, Selectivity = 1 indicates that all firing occurs during the left-associated cue odour, whereas Selectivity = −1 means that all firing occurs during right-cue odours.

Population vector analysis. To estimate the development of odour-specific representations for a whole population of cells, population vector (PV) analysis was performed as described previously[38,39]. Mean firing rates in individual 100-ms bins were pooled for cells from all animals to construct vectors for left and right-associated odours. A correlation coefficient (CC) for the two vectors was computed and then re-scaled as a PV Differential Index (PDI) to emphasize the difference between the population vectors as

$$\text{PDI} = 1 - \text{CC}$$

PDI = 0 indicates that the population vectors were identical, whereas PDI = 1 denotes that activity was maximally different between left and right-associated trials.

The chance level of the PDI was determined by a random permutation procedure using all cells recorded at that time-point in each region. One thousand permutations were performed for each cell in the sample. For each permutation trial, individual cue-sampling trials were randomly re-assigned as left or right-associated trials, maintaining the number of left and right trials identical to the original data. Population vectors were computed from the same ensemble of the cells as the original data for each of 1,000 permutations, resulting in 1,000 sets of PDI. The distribution of PDI across all 1,000 permutations in the sample was computed and finally the 95th percentile was determined as the chance level.

Firing rate maps. Position estimates were based on tracking of the LEDs on the head stage connected to the tetrode drive. For rate maps in the random foraging task, data were speed-filtered; only epochs with instantaneous running speeds of 5 cm s^{-1} or more were included.

To characterize firing fields, the position data were sorted into 2.5 cm × 2.5 cm bins. The path was smoothed with a 21-sample boxcar window filter (400 ms; 10 samples on each side). Firing rate distributions were then determined by counting the number of spikes in each bin as well as the time spent per bin. Maps for number of spikes and time were smoothed individually using a boxcar average over the surrounding 5 × 5 bins. Weights were distributed as follows:

$$\text{boxcar weights} = \begin{bmatrix} 0.0025 & 0.0125 & 0.0200 & 0.0125 & 0.0025 \\ 0.0125 & 0.0625 & 0.1000 & 0.0625 & 0.0125 \\ 0.0200 & 0.1000 & 0.1600 & 0.1000 & 0.0200 \\ 0.0125 & 0.0625 & 0.1000 & 0.0625 & 0.0125 \\ 0.0025 & 0.0125 & 0.0200 & 0.0125 & 0.0025 \end{bmatrix}$$

Spatial information. For each cell, the spatial information content in bits per spike was calculated as

$$\text{information content} = \sum_i p_i \frac{\lambda_i}{\lambda} \log_2 \frac{\lambda_i}{\lambda}$$

where λ_i is the mean firing rate of a unit in the ith bin, λ is the overall mean firing rate, and p_i is the probability of the animal being in the ith bin (occupancy in the ith bin / total recording time)[40]. An adaptive smoothing method, introduced by Skaggs *et al.*[41], was used before the calculation of information scores[29].

Place cells were defined as cells with spatial information content above the chance level for this parameter[42]. The chance level was determined for each time-point during learning in each brain region by a random permutation procedure using all cells recorded at that time-point in that region. One hundred permutations were performed for each cell in the sample. For each permutation trial, the entire sequence of spikes fired by the cell was time-shifted along the animal's path by a random interval between 20 s and 20 s less than the total length of the trial (usually 600 − 20 = 580 s), with the end of the trial wrapped to the beginning to allow for circular displacements. This procedure allowed the temporal firing structure to be retained in the shuffled data at the same time as the spatial structure was lost. Spatial information was then calculated for each shuffled map. The distribution of spatial information values across all 100 permutations of all cells in the sample was computed and finally the 95th percentile was determined. Place cells were defined as cells with spatial information scores above the 95th percentile of the distribution from shuffled data for the relevant group.

Gridness score. The structure of all rate maps was evaluated for all cells by calculating the spatial autocorrelation for each smoothed rate map[33,42,43]. The degree of spatial periodicity ('gridness score') was determined for each recorded cell by taking a circular sample of the autocorrelogram, centred on the central peak but with the central peak excluded, and comparing rotated versions of this sample[42]. Grid cells were defined as cells in which rotational symmetry-based grid scores exceeded the 95th percentile of a distribution of grid scores for shuffled recordings from the entire population of cells. Shuffling was performed in the same way as for place cells by time-shifting the spike sequence for each permutation trial. The shuffling procedure was repeated 100 times for each of the cells in the sample. Grid scores were computed for all permutations for all cells and the 95th percentile was read out from the overall distribution. Grid cells were defined as cells with grid scores higher than the 95th percentile of the grid scores of the distribution for the shuffled data.

Histology and 3D reconstruction. After receiving an overdose of pentobarbital, the rats were perfused intracardially with saline and 4% formaldehyde. The brains were then removed and stored in formaldehyde. For verification of tetrode locations, the brains were frozen, cut at 30 μm thickness, and stained with cresyl violet. For hyperdrive recordings, all tetrodes of the 14-tetrode bundle were identified, and the tip of each electrode was found by comparison with adjacent sections. For microdrive recordings, the positions of the bundle of four tetrode tips were determined. Digital photomicrographs were acquired with a Zeiss Axoimager-Z1 microscope equipped with a digital camera using AxioVision software. For CA1 recordings, all tetrodes were identified in the pyramidal cell layer of the CA1. For LEC and MEC recordings, all tetrodes were identified in layer III. In some animals with LEC or MEC microdrives, LFP recordings were moved for 100 μm to acquire additional cells after completion of T5 recordings with the original tetrode locations. In these cases, the exact position of the electrodes at the time of the original recording was extrapolated[42].

For CA1 recordings, the positions of the tetrodes were three-dimensionally reconstructed and analysed using as described previously[44]. Tetrode positions and structure of cell layers for each section in the dorsal hippocampal region were digitally registered using a computer-assisted system (Neurolucida, MBF Bioscience) according to the manufacturer's instructions. The tracing output from Neurolucida was imported into MATLAB (Mathworks) for further analyses. To place electrode positions in identical coordinates and minimize the distortions originating from sectioning and reconstruction, reconstructed neurons were linearly transformed and fitted into reference brain coordinates. A reference brain was first reconstructed. Three landmarks for transformation were used: the anterior tip of subiculum (tSUB), the anterior tip of the lateral ventricle, and the 'X'-shaped pyramidal pool of CA3 in the intermediate portion of the hippocampus[45]. These landmarks were selected because (1) they were distributed at the periphery of the dorsal hippocampus and (2) they could be uniquely defined and were unaffected by rotation of the brain. The coordinate system was defined as giving the tSUB coordinates of [0, 0, 0] in the [x (lateral), y (anterior) and z (dorsal)] directions (in μm). Individual sample brains with the tetrode tip positions were then fitted to the reference brain with regard to the above landmarks using affine (linear) transformation (translation, rotation, scaling, and shear). The surface of CA1 pyramidal cell layer was then reconstructed by interpolating reconstructed cell layer data. The major (longest) axis of the CA1 cell layer was defined as the septotemporal axis of the hippocampus. For each tetrode tip, distal–proximal (DP) distance was calculated three-dimensionally by the following procedure: a transverse plane that includes the tetrode position and is perpendicular to the septotemporal axis is determined. An intersectional curve between this transverse plane and the CA1 surface is then calculated. DP distance D_{DP} was defined as $D_{\text{DP}} = L_{\text{DT}}/L_{\text{DP}}$, where L_{DT} was the length of the curve between the distal ending point of the intersectional curve and the tetrode tip position, and L_{DP} was the length between the distal and proximal two ending points along the curve. $D_{\text{DP}} = 0$ indicates the distal border, whereas $D_{\text{DP}} = 1$ indicates the proximal border.

29. Henriksen, E. J. *et al.* Spatial representation along the proximodistal axis of CA1. *Neuron* **68,** 127–137 (2010).
30. Steward, O. Topographic organization of the projections from the entorhinal area to the hippocampal formation of the rat. *J. Comp. Neurol.* **167,** 285–314 (1976).
31. Mitra, P. P. & Pesaran, B. Analysis of dynamic brain imaging data. *Biophys. J.* **76,** 691–708 (1999).
32. Kepecs, A., Uchida, N. & Mainen, Z. F. Rapid and precise control of sniffing during olfactory discrimination in rats. *J. Neurophysiol.* **98,** 205–213 (2007).
33. Sargolini, F. *et al.* Conjunctive representation of position, direction, and velocity in entorhinal cortex. *Science* **312,** 758–762 (2006).
34. Solstad, T., Boccara, C. N., Kropff, E., Moser, M. B. & Moser, E. I. Representation of geometric borders in the entorhinal cortex. *Science* **322,** 1865–1868 (2008).
35. Hafting, T., Fyhn, M., Molden, S., Moser, M. B. & Moser, E. I. Microstructure of a spatial map in the entorhinal cortex. *Nature* **436,** 801–806 (2005).
36. Fyhn, M., Molden, S., Witter, M. P., Moser, E. I. & Moser, M. B. Spatial representation in the entorhinal cortex. *Science* **305,** 1258–1264 (2004).
37. Macmillan, N. A. & Creelman, C. D. *Detection Theory: A User's Guide* (Cambridge Univ. Press, 1991).

38. Jezek, K., Henriksen, E. J., Treves, A., Moser, E. I. & Moser, M. B. Theta-paced flickering between place-cell maps in the hippocampus. *Nature* **478,** 246–249 (2011).
39. Naya, Y. & Suzuki, W. A. Integrating what and when across the primate medial temporal lobe. *Science* **333,** 773–776 (2011).
40. Skaggs, W. E., McNaughton, B. L., Gothard, K. M. & Markus, E. J. in *Advances in Neural Processing Systems* Vol. 5 (eds Hanson, S. J., Cowan, J. D. & Giles, C. L.) 1030–1037 (Morgan Kaufmann, San Mateo, 1993).
41. Skaggs, W. E., McNaughton, B. L., Wilson, M. A. & Barnes, C. A. Theta phase precession in hippocampal neuronal populations and the compression of temporal sequences. *Hippocampus* **6,** 149–172 (1996).
42. Langston, R. F. *et al.* Development of the spatial representation system in the rat. *Science* **328,** 1576–1580 (2010).
43. Fyhn, M., Hafting, T., Treves, A., Moser, M. B. & Moser, E. I. Hippocampal remapping and grid realignment in entorhinal cortex. *Nature* **446,** 190–194 (2007).
44. Igarashi, K. M. *et al.* Parallel mitral and tufted cell pathways route distinct odor information to different targets in the olfactory cortex. *J. Neurosci.* **32,** 7970–7985 (2012).
45. Fanselow, M. S. & Dong, H. W. Are the dorsal and ventral hippocampus functionally distinct structures? *Neuron* **65,** 7–19 (2010).

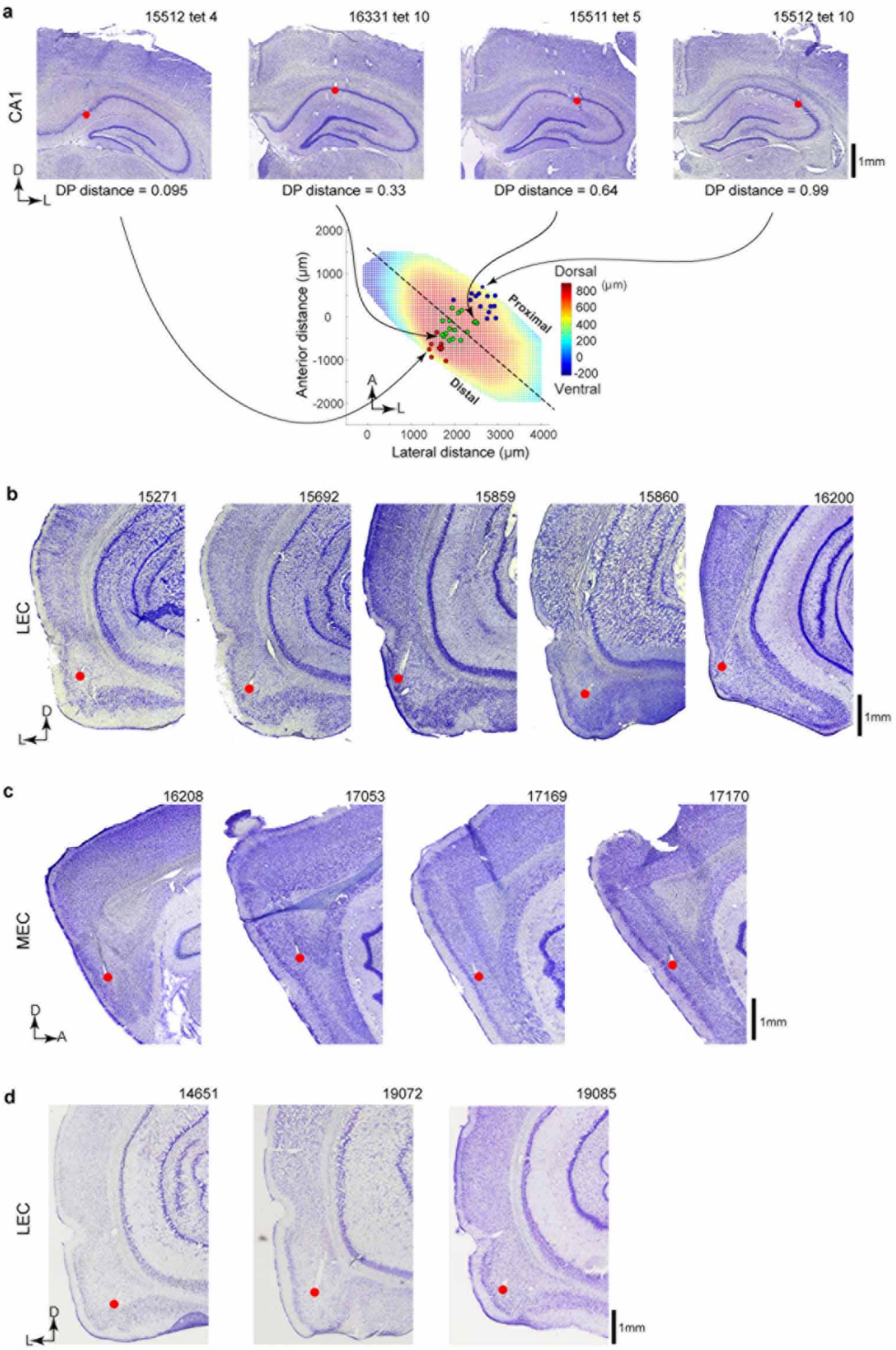

Extended Data Figure 1 | Brain sections showing recording positions in CA1, LEC and MEC. **a**, Recording positions (red) in CA1 in coronal brain sections from representative animals (top; animal and tetrode numbers indicated; distal–proximal (DP) distances as in Extended Data Fig. 5) and in a projection of a 3D reconstruction of the CA1 pyramidal cell layer (bottom; see Extended Data Fig. 5 for the full 3D reconstruction). Abscissa shows the lateral–medial axis and ordinate the anterior–posterior axis. Dorsal–ventral is colour-coded. Each dot corresponds to one recording location in distal (red), intermediate (green) and proximal (blue) parts of CA1. Stippled line indicates septotemporal axis of the hippocampus (see Supplementary Methods). **b**, Tetrode positions (red) in coronal sections through LEC for all 5 animals with simultaneous recordings in LEC and dCA1. Animal numbers are indicated. **c**, Tetrode positions (red) in sagittal sections through MEC (all 4 animals with simultaneous MEC and dCA1 recordings). **d**, Tetrode positions (red) in coronal brain sections through LEC from all 3 animals with simultaneous recordings in pCA1 and LEC. Orientation: D, dorsal; L, lateral; A, anterior.

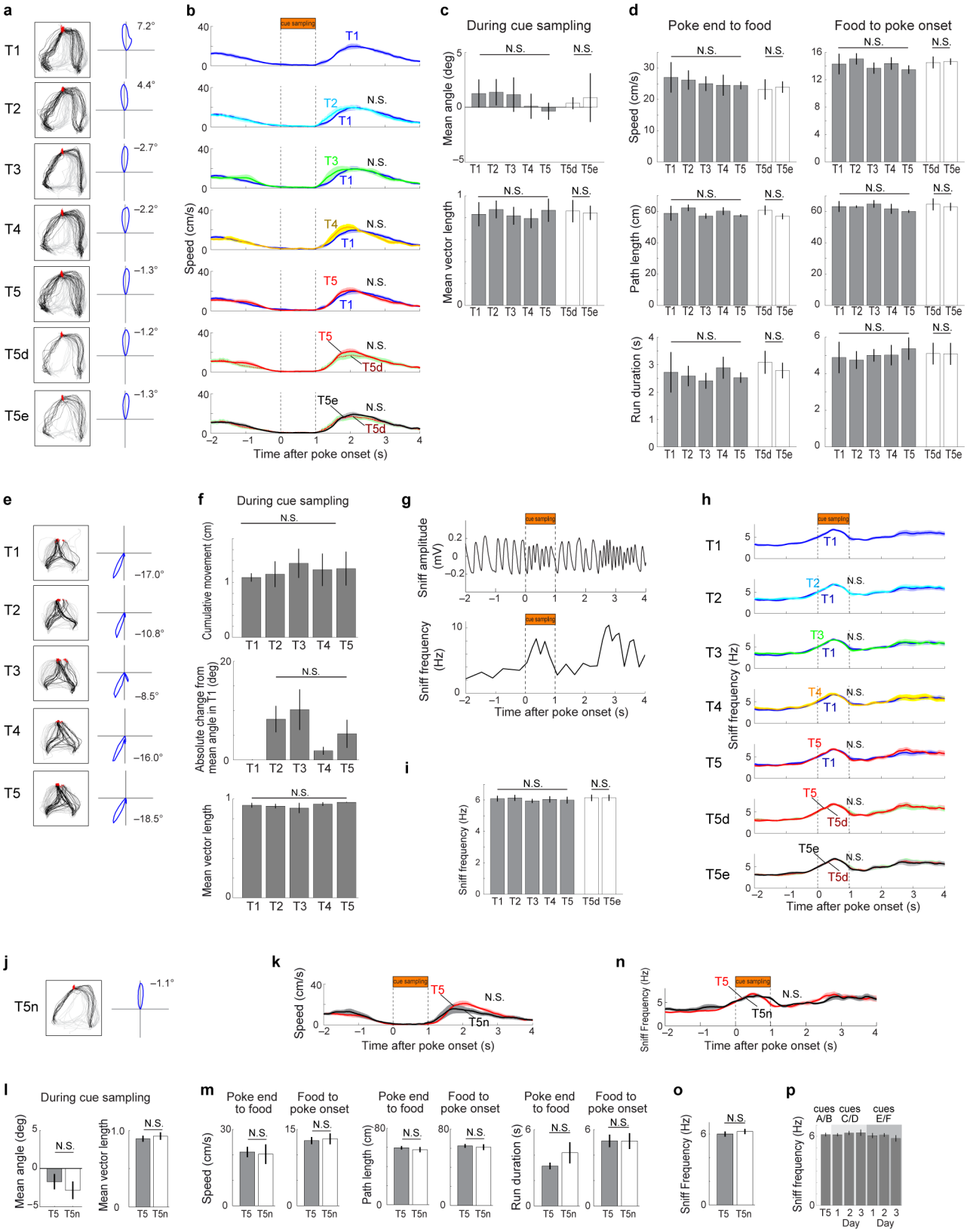

Extended Data Figure 2 | Learning was not associated with changes in motor behaviours. **a**, Left, example trajectories of one animal on sessions T1 to T5, on error trials (T5e) and on correct trials downsampled to the same number of trials as the error trials (T5d). Red parts of each trajectory indicate positions covered during the cue sampling interval, black indicates positions during runs from cue port to food cups, and grey shows positions from food cups back to the cue port. Right, polar plots showing distributions of head direction during the cue sampling interval (T1–T5, T5d and T5e, as indicated to the left). Values to the right indicate mean head angle relative to the centre of the cue port, designated as north (0°). **b**, Time course of instantaneous speed before, during and after cue sampling, averaged across 5 rats. Shading denotes s.e.m. T1 is shown at the top; T5, T5d and T5e at the bottom. For every 10-ms time bin during T2–T5, speed was compared with the corresponding bin at T1. Speeds were not significantly different from T1 at any time bin ($q > 0.05$; false discovery rate (FDR) corrected for multiple comparisons). Speed was not different at T5e and T5d. **c**, Mean head angle (top) and mean vector length for head direction (bottom) during the cue sampling interval (mean ± s.e.m. for all 5 animals). Neither head angle nor mean vector length changed significantly from T1 to T5 (repeated measures ANOVA: $F(4, 16) = 0.44$, $P = 0.78$ for mean angle; $F(4, 16) = 0.13$, $P = 0.97$ for mean vector length). There was also no change in these parameters on the error trials (T5e compared with T5d using two-tailed paired *t*-test: $t(4) = 0.70$, $P = 0.52$ for mean angle; $t(4) = 0.18$, $P = 0.87$ for mean vector length). **d**, Mean instantaneous speed (top), path length (middle) and run duration (bottom) for trajectories from cue port to food cups (left column) and from food cups to cue port (right column). None of these parameters changed significantly during learning (repeated measures ANOVA for time-points T1–T5; for cue port to food cups: $F(4, 16) = 0.14$, $P = 0.97$ for mean speed, $F(4, 16) = 0.55$, $P = 0.70$ for path length, $F(4, 16) = 0.16$, $P = 0.95$ for run duration; for food cups to cue port: $F(4, 16) = 0.35$, $P = 0.84$ for mean speed, $F(4, 16) = 0.47$, $P = 0.76$ for path length, $F(4, 16) = 0.13$, $P = 0.97$ for run duration). None of these parameters changed on error trials (T5e compared with T5d using two-tailed paired *t*-test; cue port to food cups: $t(4) = 0.31$, $P = 0.77$ for mean speed, $t(4) = 1.87$, $P = 0.52$ for path length, $t(4) = 0.91$, $P = 0.42$ for run duration; food cups to cue port: $t(4) = 0.14$, $P = 0.89$ for mean speed, $t(4) = 0.50$, $P = 0.64$ for path length, $t(4) = 0.02$, $P = 0.99$ for run duration). **e**, To check if changes in neural activity from T1 to T5 are associated with changes in body position, LEDs were attached to the back of 4 rats and LED positions were recorded from T1 to T5. Left, example trajectories of body position in one animal at different stages of learning. Red indicates body positions covered during the cue sampling interval, black indicates positions during runs from cue port to food cup, and grey show positions from food cup back to the cue port. Right, polar plots showing distribution of body direction (deflection from south) during the cue sampling interval (T1–T5). **f**, Cumulative body movement (top), mean body angle (middle) and mean vector length for body direction (bottom) during the cue sampling interval (mean ± s.e.m. of 4 animals). In the middle panel, body angle is shown as the absolute change in mean angle compared to T1, since different rats may turn in different directions. None of these parameters changed significantly from T1 to T5 (repeated measures ANOVA: $F(4, 12) = 0.77$, $P = 0.57$ for cumulative body movement; $F(3, 9) = 1.06$, $P = 0.41$ for mean angle; $F(4, 12) = 1.11$, $P = 0.40$ for mean vector length). **g**, Example recording showing changes in sniffing amplitude and frequency during cue sampling. A temperature sensor (thermocouple) was implanted in the right nostril to measure respiration (top). In each breathing cycle, inhalation is associated with decaying voltage output from the thermocouple, and exhalation with increasing voltage. Instantaneous sniff frequency was determined from the voltage change (bottom). Note that sniff frequency increased during cue sampling (between $t = 0$ s and $t = 1$ s) and when the animal approached the food cup. The food cup was reached at $t = 3.8$ s in the present example. **h**, Time course of sniff frequency averaged for 5 rats at time-points T1–T5 as well as on error trials (T5e) and correct trials down-sampled to the same number of trials (T5d). Shading denotes s.e.m. At time points T2–T5, sniff frequency was compared for every 10 ms bin with corresponding bins at T1. None of the comparisons were significantly different ($q > 0.05$; FDR corrected for multiple comparisons). Sniff frequencies between T5d and T5e were also not different. **i**, Mean sniff frequency during the cue sampling interval. Sniff frequency did not change during the course of learning (repeated measures ANOVA: $F(4, 16) = 0.24$, $P = 0.91$) or on error trials (T5e compared with T5d using two-tailed paired *t*-test, $t(4) = 0.03$, $P = 0.97$). **j**, Left, example traces showing position of the animal on non-cued control trials (T5n). Colours indicate positions during cue sampling (red), positions from cue port to food cups (black) and positions from food cups back to cue port (grey). Right, polar plot showing head direction distribution during the cue sampling period for the session shown on the left. Values on the right indicate mean head angle. The centre of the cue port is north, or 0°. **k**, Instantaneous speed on non-cued trials, averaged across 5 rats. Shading denotes s.e.m. Speed on non-cued trials (T5n) was compared at successive 10-ms bins with speed on corresponding bins of cued trials (T5). Differences were not significant at any time bin between 2 s before and 4 s after poke onset ($q > 0.05$, FDR corrected for multiple comparisons). **l**, Mean head angle (top) and mean vector length of head direction (bottom) during the cue-sampling interval. Neither head angle nor mean vector length was different from corresponding values on cued trials (two-tailed paired *t*-test, $t(4) = 1.85$, $P = 0.13$ for mean angle; $t(4) = 1.99$, $P = 0.12$ for mean vector length). **m**, Mean speed (top), path length (middle) and run duration (bottom) for trajectories from cue port to food cups (left column) and from food cups to cue port (right column). None of these parameters were different between cued and non-cued tasks (two-tailed paired *t*-test; cue port to food cup movements: $t(4) = 0.16$, $P = 0.88$ for mean speed, $t(4) = 0.50$, $P = 0.64$ for path length, $t(4) = 1.03$, $P = 0.36$ for run duration; food cup to cue port movements: $t(4) = 0.21$, $P = 0.84$ for mean speed, $t(4) = 0.30$, $P = 0.78$ for path length, $t(4) = 0.44$, $P = 0.68$ for run duration). **n**, Sniff frequency at the cue port on non-cued trials, averaged across 5 rats. Frequency on cued trials is shown as a reference. Shading denotes s.e.m. Sniff frequency was compared at successive 10-ms bins between T5 and T5n. Differences were not significant at any time between 2 s before and 4 s after poke onset ($q > 0.05$; FDR corrected for multiple comparisons). **o**, Mean sniff frequency during the cue sampling period was not different between T5 and T5n (two-tailed paired *t*-test, $t(4) = 0.89$, $P = 0.43$). **p**, Mean sniff frequency during the cue sampling interval in novel odour trials. Sniff frequency did not change over the course of trials with novel odours (repeated measures ANOVA: $F(6, 18) = 0.77$, $P = 0.60$).

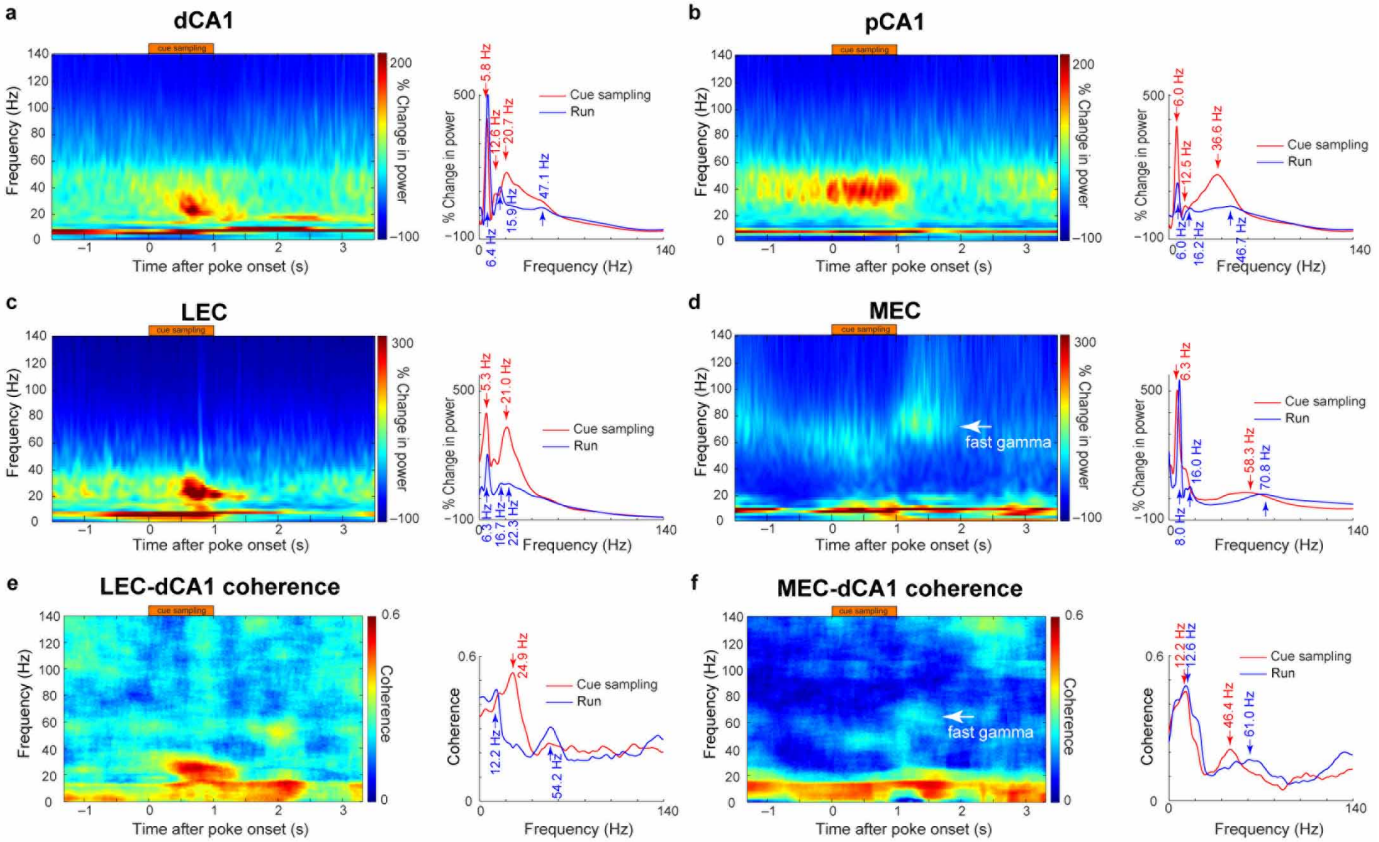

Extended Data Figure 3 | Power and coherence over a broader spectrum of frequencies in dCA1 and LEC at the end of training. **a–d**, Time-resolved power spectra averaged across tetrodes in **a**, dCA1 ($n = 9$ tetrodes), **b**, pCA1 ($n = 14$ tetrodes), **c**, LEC ($n = 10$ tetrodes) and **d**, MEC ($n = 8$ tetrodes), as in Fig. 1e and g, but for a broader band of the frequency spectrum (0–140 Hz). Power is shown as percentage change from power during the pre-cue period. dCA1 and pCA1 data are from the same animals (rats with tetrodes along the entire proximodistal CA1 axis), whereas LEC and MEC data are from separate animals (5 and 4 rats, respectively). Right panels show mean power for frequencies up to 140 Hz during cue sampling (red) and during running from cue port to food cups (blue). Peak frequencies are indicated. In CA1, the mean power in the 20–40-Hz frequency band increased from $(1.07 \pm 0.04) \times 10^{-3}$ before cue sampling to $(1.36 \pm 0.05) \times 10^{-3}$ during cue sampling and then reverted to $(0.89 \pm 0.05) \times 10^{-3}$ mV^2 after cue sampling (repeated measures ANOVA: $F(2, 78) = 118$, $P < 0.001$). In LEC, the power was $(1.05 \pm 0.12) \times 10^{-3}$, $(1.62 \pm 0.16) \times 10^{-3}$ and $(0.78 \pm 0.08) \times 10^{-3}$ mV^2, respectively ($F(2, 18) = 67.1$, $P < 0.001$). **e**, **f**, Time-resolved coherence spectra averaged across tetrode pairs in LEC and dCA1 (**e**) and in MEC and dCA1 (**f**), as shown in Fig. 1h, but across a broader band of the frequency spectrum (same animals as in **c** and **d**; data are averaged across all EC-dCA1 tetrode pairs). Note that, during running, MEC shows fast gamma oscillations (60–100 Hz) that are coherent with dCA1 LFPs (arrows). Right panels show mean coherence spectra during cue sampling (red) and during running (blue), with peak frequencies indicated. LEC did not show fast gamma oscillations.

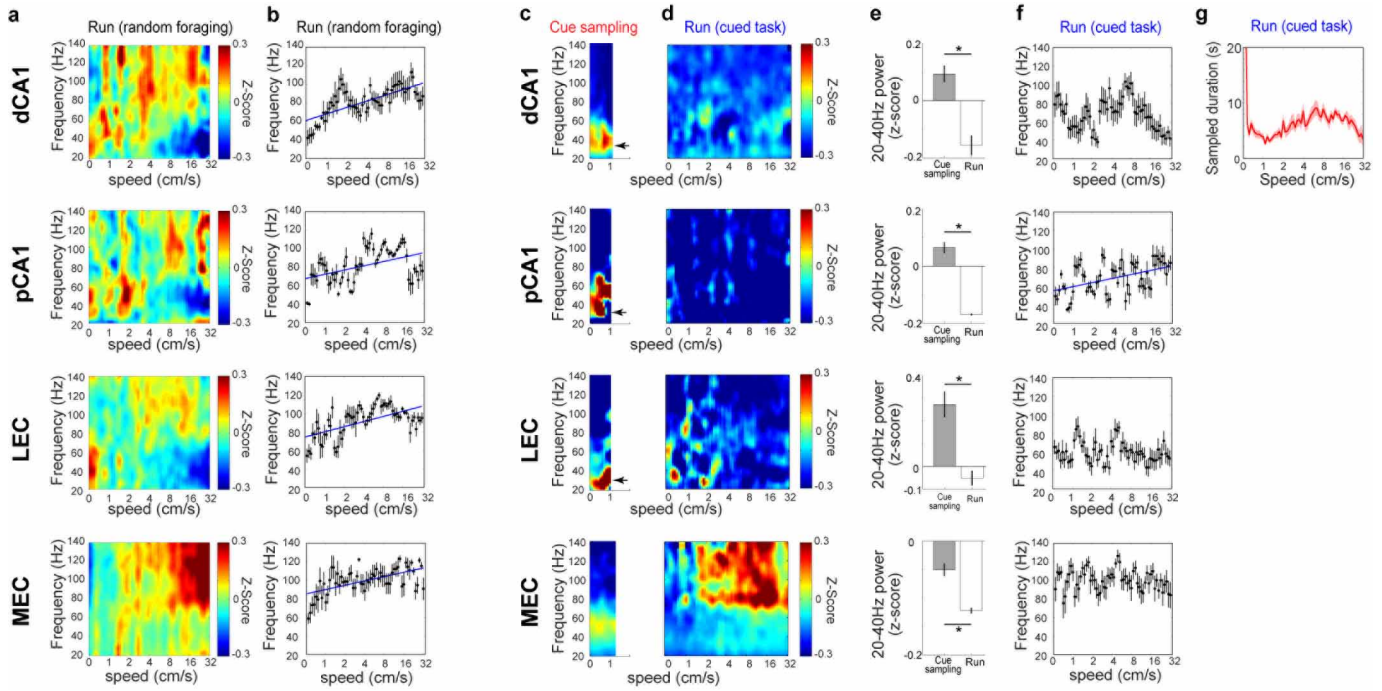

Extended Data Figure 4 | Effect of running speed on oscillation frequency. **a**, Power spectra of oscillations in dCA1, pCA1, LEC and MEC as a function of running speed at T5 during random foraging in the 1 × 1 m square box. Power is normalized at each frequency bin and shown as a z-score[18]. Data were averaged across 9 (dCA1), 14 (pCA1), 10 (LEC) and 8 (MEC) tetrodes from 5 dCA1 and pCA1, 5 LEC and 4 MEC rats, respectively. **b**, Peak oscillation frequency (mean ± s.e.m. for all tetrodes) as a function of speed bin in **a**. As in previous work[18], a significant correlation was observed between speed and peak frequency of oscillations in the 20–140-Hz range ($P < 0.001$; $r(58) = 0.71, 0.44, 0.60$ and 0.59 for dCA1, pCA1, LEC and MEC, respectively). **c**, **d**, Speed–frequency relationship in the cue-place association task. Same tetrodes as in **a**. Data were plotted during the cue sampling period (**c**) and during subsequent running from the cue sampling port to the food cups (**d**). Note that during cue sampling, speed was minimal (~0–1 cm s^{-1}). Strong 20–40-Hz oscillations were observed in dCA1, pCA1 and LEC (arrows in **c**) but not at similar speeds during running (**d**). **e**, In all four brain regions (dCA1, pCA1, LEC and MEC), the power at very low speeds (0–1 cm s^{-1}) was significantly stronger during cue sampling than during running (paired t-test, $P < 0.01$; $t(8) = 3.9$, $t(13) = 13.7$, $t(9) = 13.4$ and $t(7) = 4.5$ for dCA1, pCA1, LEC and MEC, respectively), suggesting 20–40-Hz oscillations do not reflect low speed as such. **f**, During running from cue port to food cups, a significant positive correlation between speed and frequency was observed only in pCA1($P < 0.001$, $r(58) = 0.48$). **g**, Time spent in each speed bin during the running part of the cued task (means ± s.e.m. for all 14 rats). Note that all speed bins (including low speeds) were sampled for 2.5 s or more.

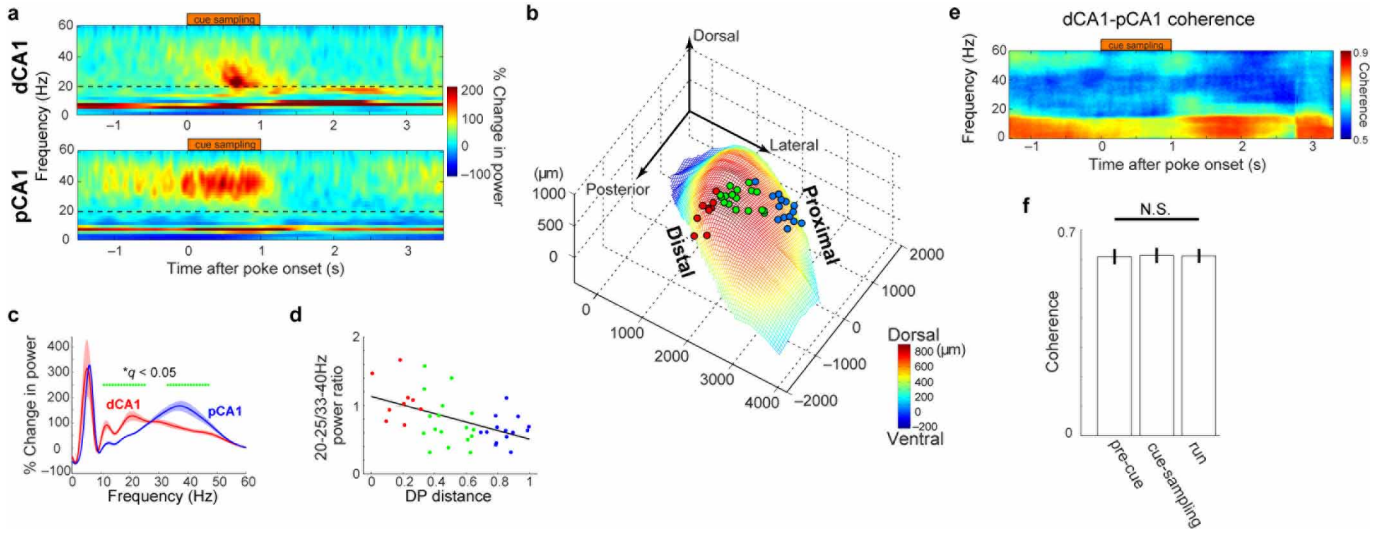

Extended Data Figure 5 | 20–40-Hz oscillations in dCA1 and pCA1 are functionally decoupled. **a**, Time-resolved power spectra averaged across all tetrodes in the distal one-third of CA1 (dCA1, top) as well as the proximal one-third (pCA1, bottom) (9 and 14 recording sites, respectively). Data were pooled over 5 rats with hyperdrive implants spanning a wide transverse range of CA1. To control for impedance differences between tetrodes, LFP power during cue sampling was normalized, for each tetrode, to power during the pre-cue period when the animal was stationary at the odour port before the cue was delivered. Normalized power was averaged across tetrodes. Time $t = 0$ indicates cue onset. **b**, Positions of all tetrodes from which data were recorded in **a**, plotted in a 3D reconstruction of the CA1 cell layer. Distance from the anterior tip of subiculum is shown in micrometres. Position on the distal–proximal (DP) axis (0, distal; 1, proximal; see Supplementary Methods) was calculated in 3D space for each tetrode. CA1 tetrodes were grouped into distal (red point), intermediate (green point) and proximal (blue point) groups, each corresponding to one-third of the DP axis. **c**, Power spectra of LFP averaged over tetrodes in distal and proximal one-thirds of CA1 during cue sampling. Power is shown as percentage change from the pre-cue level. During cue sampling, power in the lower part of the 20–40-Hz band was stronger in dCA1 than pCA1 (11–25 Hz, green dots; $q < 0.05$; false discovery rate (FDR) corrected for 60 multiple comparisons at 1–60 Hz using 1 Hz bins, $q < 0.05$), whereas power in the higher part was lower in dCA1 (33–47 Hz, green dots; $q < 0.05$). **d**, To compare power in the lower and higher parts of the 20–40-Hz oscillation across the DP axis in CA1, the ratio of power in the slower part (20–25 Hz) and the faster part (33–40 Hz) was plotted as a function of DP distance. Each dot refers to one tetrode. Red, distal one-third; green, intermediate; blue, proximal one-third. Low/high power ratio was negatively correlated with DP distance ($r(38) = -0.50$, $P < 0.001$). **e**, Time-resolved coherence spectrum for dCA1 versus pCA1. Data were averaged over 28 recording pairs in dCA1 and pCA1 from animals with tetrodes in both regions. **f**, Mean coherence between dCA1 and pCA1. Note lack of change in 20–40-Hz coherence during cue sampling compared to pre-cue or run periods (repeated measures ANOVA, $F(2, 54) = 0.75$, $P = 0.48$).

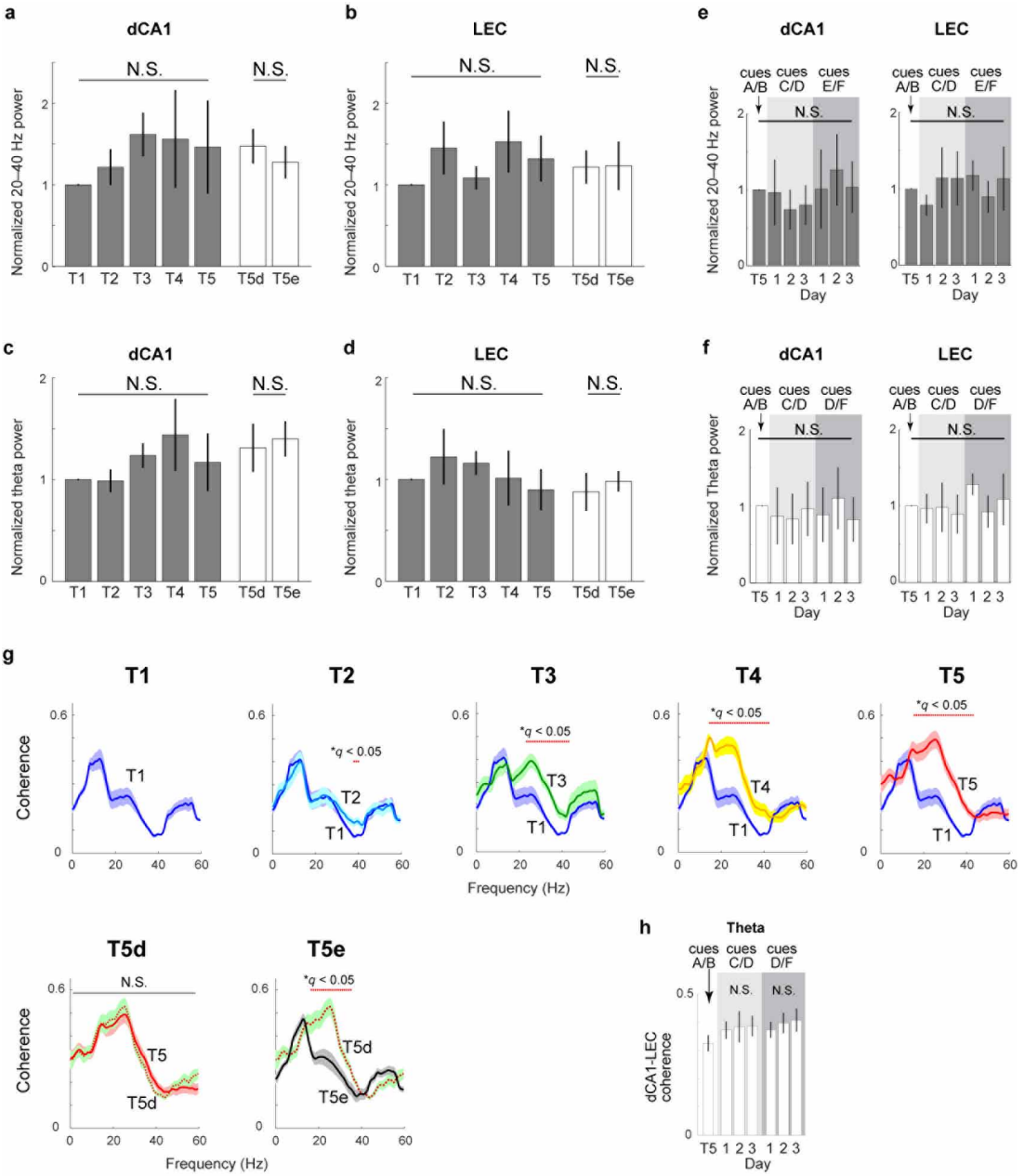

Extended Data Figure 6 | Comparison of power and coherence development during learning. **a**, **b**, Power of 20–40-Hz oscillations in dCA1 (**a**, $n = 10$ tetrodes) and LEC (**b**, $n = 10$ tetrodes) from 5 rats at time points T1–T5, on error trials at T5 (T5e) and at T5 after down-sampling (T5d), shown as values normalized by power at time point T1. Power of 20–40-Hz oscillations did not change significantly during the course of learning (repeated measures ANOVA: $F(4, 36) = 0.72$, $P = 0.58$ for dCA1; $F(4, 36) = 1.71$, $P = 0.17$ for LEC). Power on error trials (T5e) was not significantly different from correct trials (T5d; two-tailed paired t-test, $t(9) = 1.40$, $P = 0.20$ for dCA1; $t(9) = 0.06$, $P = 0.94$ for LEC). **c**, **d**, Power of theta oscillations in dCA1 (**c**) and LEC (**d**). Theta power did not change during learning (repeated measures ANOVA: $F(4, 36) = 0.90$, $P = 0.47$ for dCA1; $F(4, 36) = 0.63$, $P = 0.64$ for LEC). Theta power on error trials was not different from correct trials (two-tailed paired t-test, $t(9) = 0.24$, $P = 0.82$ for dCA1; $t(9) = 0.40$, $P = 0.70$ for LEC). **e**, Power of 20–40-Hz oscillations in dCA1 (left, $n = 8$ tetrodes) and LEC (right, $n = 8$ tetrodes) at the end of training with the original odours (A/B; time point T5), and with odours C/D and E/F (mean ± s.e.m.) (4 rats). Power of the 20–40-Hz oscillations did not change significantly with the new odours, neither between T5 and the first day with C/D or E/F ($t(7) < 0.5$, $P > 0.6$ for CA1, $t(7) < 0.9$, $P > 0.4$ for LEC) nor during the course of learning with C/D and E/F (repeated measures ANOVA: $F(6, 42) = 0.34$, $P = 0.91$ for dCA1; $F(6, 42) = 0.44$, $P = 0.85$ for LEC). **f**, Power of theta oscillations in dCA1 (left) and LEC (right) (mean ± s.e.m.). There was no significant change in the power of theta (repeated measures ANOVA: $F(6, 42) = 0.13$, $P = 0.99$ for dCA1; $F(6, 42) = 0.71$, $P = 0.64$ for LEC). **g**, Mean of LEC–dCA1 coherence spectra during cue sampling at successive time points during learning (T1–T5) and on error trials (T5e) and down-sampled correct trials (T5d), plotted in the same way as the time-resolved coherence spectra in Fig. 2b ($n = 20$ recording pairs from 5 rats). Dots above spectra denote frequencies with significant difference (FDR corrected for 62 multiple comparisons at 0–60 Hz, $q < 0.05$). **h**, Coherence averaged across the theta-frequency band during cue sampling in novel odour trials. No change was observed for coherence in the theta frequency band (repeated measures ANOVA: $F(2, 30) = 0.02$, $P = 0.98$ for cues C/D and $F(2, 30) = 0.25$, $P = 0.78$ for cues E/F).

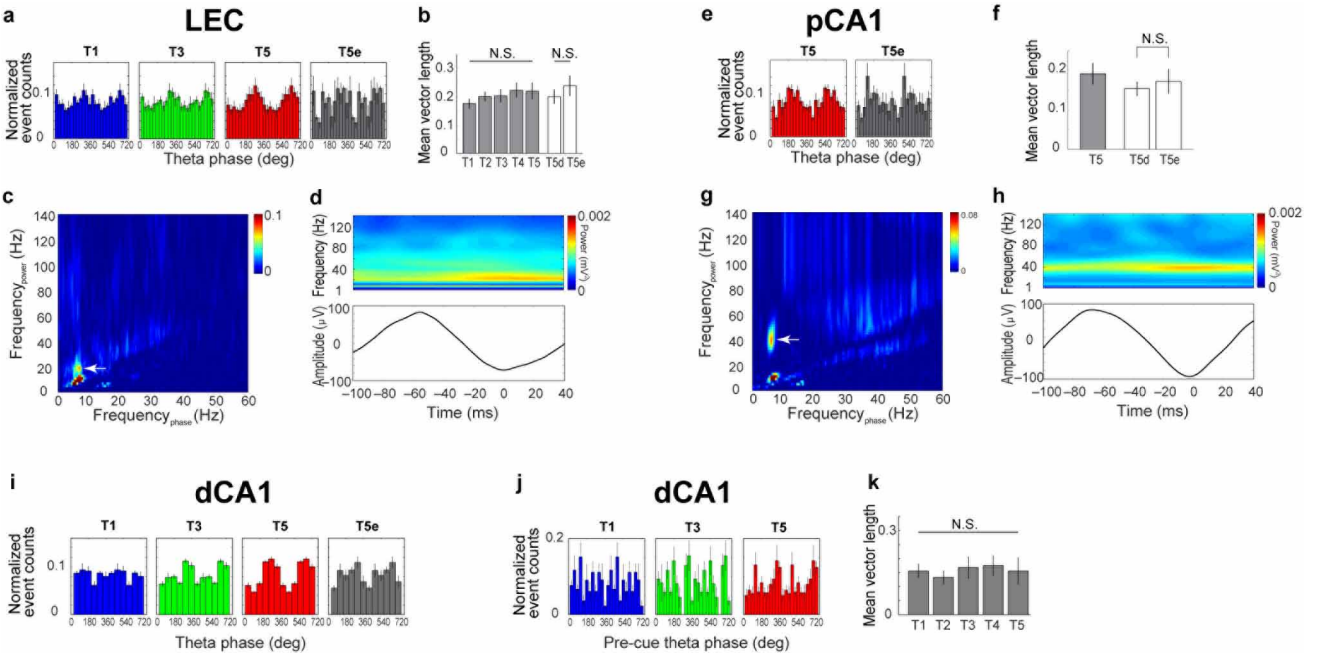

Extended Data Figure 7 | Cross-frequency coupling of 20–40-Hz oscillations to local theta oscillations in LEC and pCA1. a–d, Relationship of 20–40-Hz oscillations in LEC to phase of local theta oscillations, plotted as in Fig. 2d–g ($n = 10$ tetrodes from 5 rats). **a**, Theta phase distribution of 20–40-Hz oscillation maxima at T1, T3, T5 and on error trials at T5 (T5e). 0° was defined as the trough of the theta cycle. Note that theta oscillations exist in LEC and that 20–40-Hz oscillations are moderately phase-coupled with theta oscillations already at T1. **b**, Mean vector length calculated from theta phase distribution of 20–40-Hz oscillation maxima at T1–T5. The degree of cross-frequency coupling did not change significantly across the learning period (T1–T5, repeated measures ANOVA: $F(4, 36) = 1.7$, $P = 0.17$). No difference was observed on error trials (T5e, compared with T5d using a two-tailed paired t-test, $t(9) = 0.78$, $P = 0.45$). **c**, Representative cross-frequency coherence plot showing for LEC that power of 20–40 Hz oscillations (y-axis) is modulated by theta phase (x-axis) during cue sampling at T5. Coupling strength is colour-coded (dark blue, no coupling; red, maximal coupling). **d**, Top, time-resolved power spectrum averaged across all theta cycles with 20–40-Hz oscillations at T5 in LFP from 10 tetrodes in all 5 rats. $t = 0$ corresponds to the theta trough. Bottom, averaged unfiltered theta cycle. 20–40-Hz oscillations occurred at the falling phase of the theta wave. **e–h**, Similar plots for pCA1 ($n = 14$ tetrodes from 5 rats; **e**, theta phase distribution; **f**, mean vector length; **g**, cross-frequency coherence plot; **h**, time-resolved power spectrum). Animals with implants in pCA1 were recorded only after the completion of learning, that is, only at T5. In pCA1, oscillations at ~30–50-Hz were phase-coupled with theta oscillations. The degree of coupling did not change on error trials (two-tailed paired t-test, $t(13) = 1.29$, $P = 0.22$). **i**, Same plots as in Fig. 2f, but with wider 60° bins. The diagram shows the relationship of 20–40-Hz oscillations in dCA1 to the phase of local theta oscillations ($n = 10$ tetrodes from 5 rats). The use of wider bins did not change the results. Significant cross-correlations between cell pairs in LEC and CA1 were not found, as expected due to the sparse connectivity between cell pairs in these areas[13]. **j**, Theta phase distribution of 20–40-Hz oscillation maxima for LFP from dCA1 as in Fig. 2f, but during the pre-cue period, at time points T1, T3, T5 ($n = 10$ tetrodes from 5 rats, means ± s.e.m.). **k**, Mean vector length calculated from theta phase distributions of 20–40-Hz oscillation maxima during the pre-cue period did not change during the course of training (repeated measures ANOVA: $F(4, 36) = 0.26$, $P = 0.90$; $n = 10$ tetrodes from 5 rats). Vector lengths during cue sampling was increased compared to the pre-cue period at T5 (paired t-test, $P < 0.05$; $t(9) = 2.5$) but not at T1–T4 ($P > 0.05$; $t(9) < 1.9$).

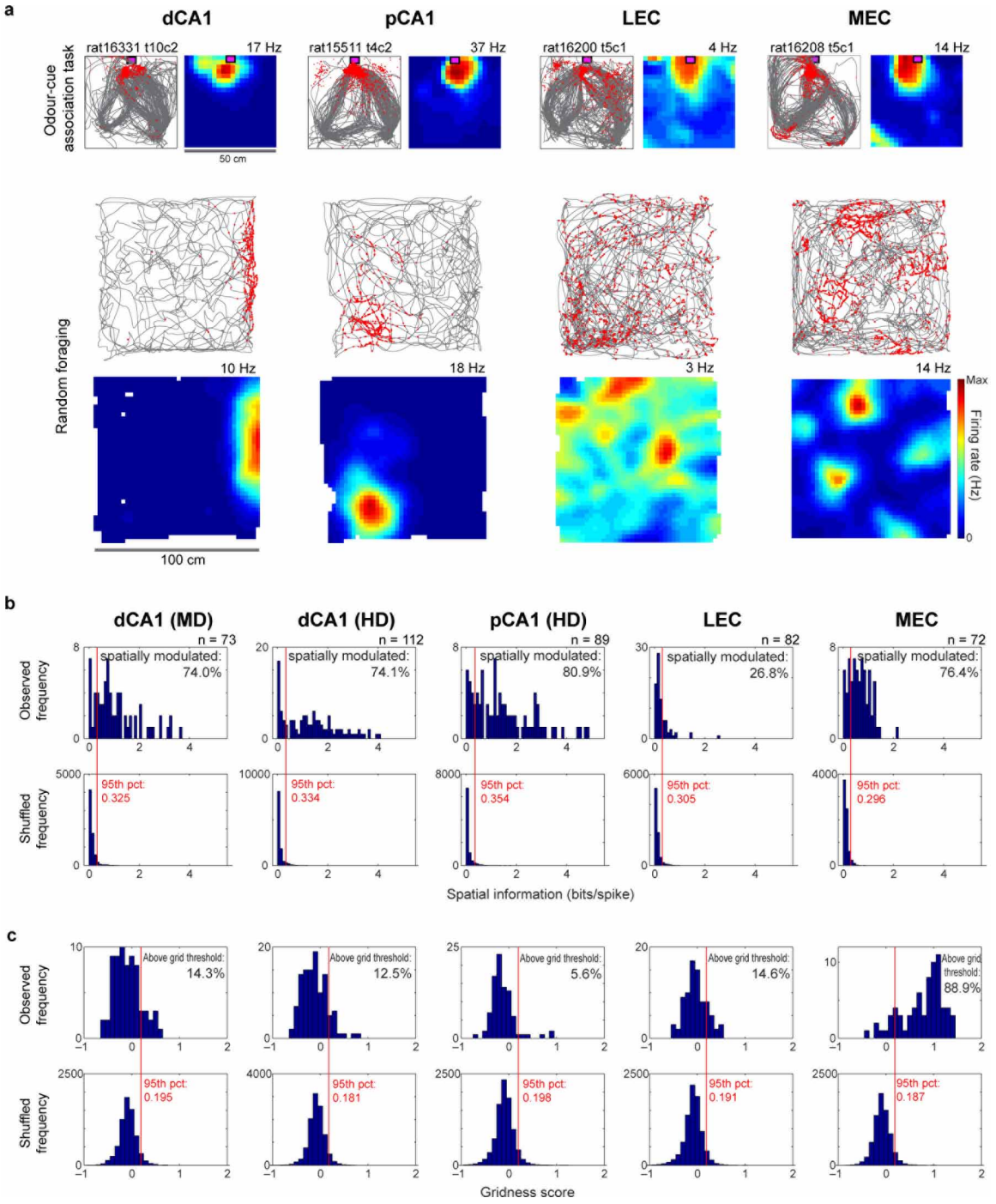

Extended Data Figure 8 | A large fraction of CA1 and MEC cells with activity at the cue port were place cells and grid cells, respectively. **a**, Spatial distribution of firing in example cells with cue-port activity recorded in dCA1, pCA1, LEC or MEC in either the odour–cue association task (top) or a random foraging task in a 1 m square box (bottom). Each column shows results for one representative cell. For each cell, spike position (red) is overlaid on the trajectory of the rat (grey) at the top and a colour-coded frequency map is shown at the bottom. Red is maximum firing rate, as indicated by the scale bar. Rat number, tetrode number (*t*) and cell number (*c*) are indicated above each path diagram. Peak frequencies are indicated at the top right of the colour map. Note that dCA1/pCA1 and MEC cells had clearly distinguishable place fields or grid fields in the foraging task, whereas the LEC cell showed no clear spatial modulation. **b**, Top, distribution of spatial information scores calculated from firing rate distributions in the random foraging task for cells with cue-port activity in dCA1, pCA1, LEC and MEC. Results in dCA1 are shown for both microdrive (MD) and hyperdrive (HD) implants. Bottom, distribution of shuffled data based on 100 permutations per cell. Red lines indicate 95th percentile value (chance level) for a distribution based on all permutations in each area. 95th percentile value is indicated in red. Percentage of cells that exceeded chance level is shown for each region. Note that 74% and 81% of the cue-port cells were spatially modulated in dCA1 and pCA1, respectively, that is, they were place cells[45]. **c**, As in **b**, but for the distribution of gridness scores. Note that 89% of cue port cells in MEC had gridness scores that exceeded chance level and so were defined as grid cells[45].

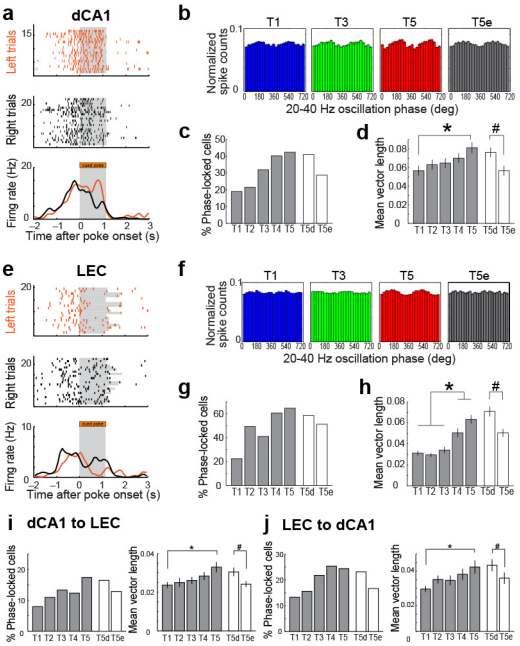

Extended Data Figure 9 | Phase-locking of individual neurons to the 20–40-Hz rhythm. **a**, Raster plots showing cue-port activity of example dCA1 cell on successive trials at T5. Rows correspond to individual trials; ticks indicate spikes. Top, trials with food in left cup; middle, trials with food in right cup; bottom, peri-stimulus time histogram (PSTH); orange, left-predicting trials; black, right-predicting trials. Between T1 and T5, the number of dCA1 cells with mean rates above 1 Hz during the cue interval ranged from 63 to 75 (5 rats). **b**, Spike-time distribution for dCA1 principal cells with cue-port activity across phase of local 20–40-Hz oscillation at T1–T5 and T5e. **c**, **d**, Percentage of significantly phase-locked cells (**c**) and mean vector length of distribution in **b** (**d**), averaged across dCA1 cells with cue-port activity. T5d as in Fig. 2c. $*^{\#}$, as in Fig. 2c. **e**–**h**, LEC cells, as in **a**–**d**. Between T1 and T5, the number of LEC cells with mean rates above 1 Hz during the cue interval ranged from 76 to 82 (5 rats). The number of cue-port cells phase-locked to the local 20–40-Hz LFP increased significantly from T1 to T5 in both dCA1 and LEC (main text) and there was a significant increase in the phase locking of each cell (ANOVA for mean vector length: dCA1: $F(4, 348) = 2.81$, $P = 0.026$; LEC: $F(4, 383) = 21.0$, $P < 0.001$). On error trials, the mean vector for the spike-phase distribution decreased in both dCA1 and LEC (dCA1: two-tailed paired t-test, $t(72) = 2.97$, $P = 0.004$; LEC: $t(81) = 4.05$, $P < 0.001$). **i**, **j**, Interregional phase-locking of individual dCA1 and LEC cells. **i**, Phase-locking of dCA1 spikes as shown in **c** and **d**, but against 20?40-Hz oscillations in LEC. Left, percentage of significantly phase-locked cells. Right, mean vector length of the spike-phase distribution. The percentage of cells that was significantly phase-locked to the oscillations increased from 7.9 at T1 to 17.4 at T5 ($P < 0.005$; binomial test with Bonferroni correction). This increase was matched by an increase in the mean vector length of the spike-phase distribution (ANOVA for mean vector length: $F(4, 348) = 2.8$, $P = 0.03$). T5e and T5d indicate T5 error trials and down-sampled correct T5 trials, respectively. Mean vector length on T5e was significantly reduced compared to T5d (two-tailed paired t-test, $t(72) = 2.60$, $P = 0.011$). **j**, Phase-locking of LEC spikes as shown in **g** and **h**, but against 20–40-Hz oscillations in dCA1. The percentage of LEC cells significantly phase-locked to 20–40-Hz oscillations in dCA1 increased from 13.3 at T1 to 24.4 at T5 ($P < 0.005$). This was accompanied by a significant increase in the mean vector length of the spike-phase distribution ($F(4, 383) = 2.7$, $P = 0.03$). Mean vector length on error trials (T5e) decreased significantly compared to down-sampled correct trials (T5d; two-tailed paired t-test, $t(81) = 2.42$, $P = 0.017$). $*P < 0.05$, Bonferroni post-hoc test; $^{\#}P < 0.05$, paired t-test.

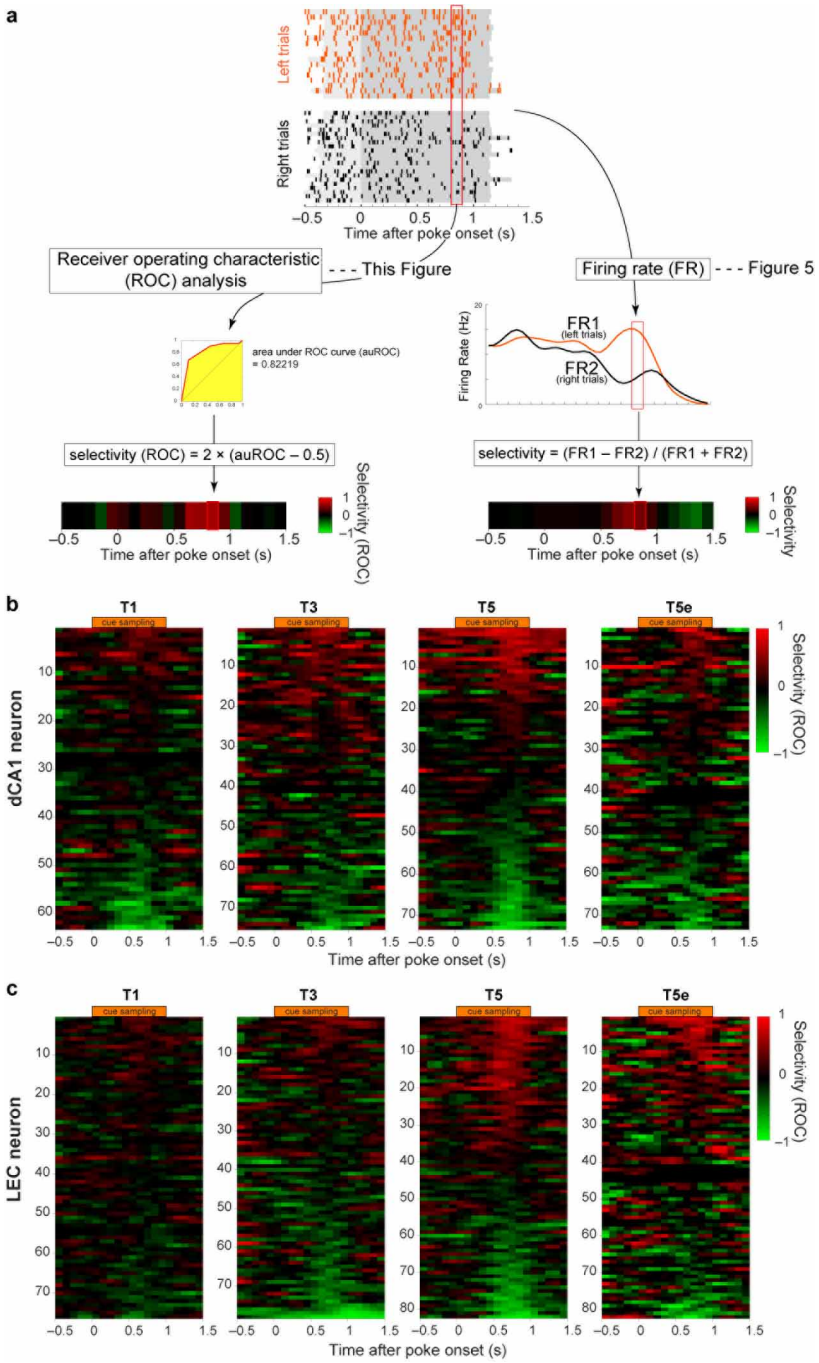

Extended Data Figure 10 | ROC-based and firing rate-based analysis of odour-specific representations in dCA1 and LEC. **a**, Schematic representation of odour-type spike representations based on receiver operating characteristic (ROC) analysis (left) and direct comparison of firing rates (right). Odour-specific representation was assessed using the metric Selectivity. Selectivity was computed by comparing firing rates during sampling periods for left-associated and right-associated cues in successive 100-ms bins: Selectivity was first expressed as (FR1 − FR2)/(FR1 + FR2), where FR1 and FR2 are mean firing rates for multiple trials on individual 100-ms bins during left- and right-associated cue samplings, respectively. To confirm the development of odour-specific representations, we subsequently computed Selectivity using ROC analysis, a method based on signal detection theory: Selectivity (ROC) was computed as 2 × (auROC − 0.5), where auROC is the area under the ROC curve computed from spike numbers for left and right trials on individual 100-ms bins. After scaling, for both Selectivity metrics, Selectivity = 1 indicates that the cell fired only on left-associated odour trials, whereas Selectivity = –1 denotes firing only on right-associated odour trials. **b**, Trial-type representations for all dCA1 cells with activity at the cue port shown as in Fig. 4a but using ROC analysis. Note development of selectivity also with this method. **c**, As in **b**, but for LEC cells.